Available online at www.sciencedirect.com

ScienceDirect

Comput. Methods Appl. Mech. Engrg. 341 (2018) 888–916

Computer methods in applied mechanics and engineering

www.elsevier.com/locate/cma

A new visco-plastic self-consistent formulation implicit in dislocation-based hardening within implicit finite elements: Application to high strain rate and impact deformation of tantalum

Miroslav Zecevic, Marko Knezevic*

Department of Mechanical Engineering, University of New Hampshire, Durham, NH 03824, USA

Received 6 March 2018; received in revised form 22 June 2018; accepted 24 July 2018
Available online 27 July 2018

Highlights

- A microstructure-based modeling framework for high-strain-rate deformation is presented.
- Visco-plastic self-consistent model implicit in dislocation-based hardening is developed.
- Spherical linear interpolation in the space of quaternions is used for interpolation of texture.
- The multi-level model is used to simulate the Taylor impact test on a cylinder of tantalum.
- Texture evolution, anisotropic plastic flow, and geometrical changes are predicted.

Abstract

Modeling deformation processes of materials under high strain rate and impact conditions in which the strain rates vary spatiotemporally over several orders of magnitude is challenging, especially in terms of constitutive description. Visco-plastic power-law flow rule, commonly used within crystal plasticity constitutive models, usually introduces superfluous strain rate effects, entering numerically via the slip activation criterion, which result in artificially high flow stress predictions under high strain rate deformation conditions. This paper presents a novel, implicit finite element implementation of a visco-plastic self-consistent polycrystal model that is implicit in dislocation-based hardening with removed strain rate sensitivity introduced by the power-law flow rule. In the model, the strain rate dependence of the flow stress is defined solely by the rate sensitivity of Peierls stress and the evolution of dislocation density within the hardening law, enabling the prediction of high strain rate and impact deformation. As a result, the predicted flow stress is accurate in its magnitude. The physically based strain rate and temperature sensitive model also features, in addition to Schmid, the non-Schmid activation contribution for slip, which is necessary for understanding and modeling the plastic deformation of body-centered cubic metals. The model is calibrated to simulate the strain rate- and temperature-sensitive monotonic deformation of tantalum and is subsequently applied to a Taylor impact test of the same material. Since the impact simulation required remeshing and interpolation of state variables, the spherical linear interpolation algorithm in the space of quaternions is implemented to facilitate the interpolation of texture. Predictions of the simulation were found to

---

* Correspondence to: University of New Hampshire, Department of Mechanical Engineering, 33 Academic Way, Kingsbury Hall, W119, Durham, NH 03824, USA.

E-mail address: marko.knezevic@unh.edu (M. Knezevic).

https://doi.org/10.1016/j.cma.2018.07.027

compare favorably with experimental measurements of post-test geometrical changes and texture evolution. The implementation and insights from these predictions are presented and discussed in the paper.

Keywords: Microstructures; Anisotropic material; Crystal plasticity; Finite elements; Impact testing

1. Introduction

Body-centered-cubic (BCC) refractory metals often operate under extreme mechanical and thermal conditions in applications such as anti-armor systems, missile bodies, space vehicle components (including vanes and nozzles that guide propulsion in rocket motors), aircraft structural components (including aircraft engines and engine parts), particle accelerators, electronic heat sinks, and heat treating and glass-melting furnaces [1–4]. Tantalum (Ta) belongs to the group of the refractory metals, which are known to exhibit strong temperature and strain rate dependent mechanical behavior [5–8].

Crystal plasticity constitutive theories have been developed and utilized over the past several decades to physically describe the behavior of metals by accounting for the details of their microstructure and the crystallography of the prevalent grain-scale deformation mechanisms [9–13]. Such theories facilitate a deeper understanding of the deformation behavior of polycrystalline metals and allow more accurate simulations of metal fabrication processes, when compared to the commonly used phenomenological plasticity models [14–18]. The predictions of the mechanical response and concomitant microstructure evolution of metallic materials under high strain rate and impact are critically important for the evaluation of metallic components in service and during their fabrication on a computer rather than the shop floor. The present paper is concerned with the development of more accurate descriptions of the deformation behavior of materials under high strain rate and high temperature, as well as the integration of such descriptions into the finite element (FE) framework to facilitate predictions of microstructure and deformed geometries. The stress needed to activate crystallographic slip depends on strain-rate and temperature and evolves with strain as dislocations interact and become stored in the crystal. Therefore, the deformation response under high strain rate and temperature conditions can be better understood and predicted with knowledge of crystallography of the deformation mechanisms and their contribution to microstructure evolution.

Taylor impact testing is used for determining dynamic yield stresses of polycrystalline metals [19]. The same test was useful in validating various constitutive laws for high strain rate deformation of metals because the metal undergoes a wide range of strain rates and strain levels during the test [20–22]. The test involves propelling a cylindrical specimen at a rigid target. The shape changes, and the microstructure can be characterized. As a result of the cylinder's highly heterogeneous deformation, the underlying microstructure can substantially vary throughout the cylinder.

Several classical plasticity models have been developed to describe the temperature and strain rate dependent behaviors of various metals, including BCC. In the Johnson-Cook model, the von Mises flow stress is expressed as a function of strain rate and temperature [23]. Later, Zerilli and Armstrong proposed a different strain rate and temperature sensitive analytical expression for flow stress, motivated by dislocation mechanics, and they applied the model specifically to simulate Ta behavior [24,25]. However, both formulations are largely empirical. Models known as the internal state variables (ISV) models, with parameters therein as a function of the strain-rate and temperature, have also been used in large deformation of metals [26]. However, accuracy of ISV models depends on the expense of a laborious tabulation of model parameters from experiments. More advanced models accounting for thermal activation of dislocations in a largely phenomenological manner, known as the Steinberg–Guinan [27] and Preston–Tonks–Wallace [28] models, have reproduced the behavior of Ta at a broad range of temperatures and strain rates. However, these models rely on fitting to macroscopic data while not explicitly considering the deformation physics at the level of crystallographic slip systems. The mechanical threshold stress (MTS) model, originally proposed by Follansbee and Kocks [29], was used for modeling dynamic deformation of Ta [6,30]. The main drawback of the above-described models is that they only capture the rate and temperature sensitive behavior of flow stress. The shape of the yield surface remains constant throughout the deformation process regardless of the microstructural changes happening within the material (e.g. texture evolution, twinning), which can greatly affect the anisotropy of the response. Continuum anisotropic yield surfaces, which evolve during deformation, specifically developed to account for plastic anisotropy and tension–compression asymmetry incorporated into a FE framework, represent an attractive alternative mainly due to their computational efficiency and accuracy [31,32]. These models have been successfully applied to predict the deformation and geometric changes of the Taylor impact specimens. However, evolution of the yield surface is captured for only one strain path while the deformation within the Taylor cylinder is very heterogeneous. Therefore, the evolution of the yield surface will be inappropriate for large number of points because their strain history is different from the one to which the yield surface was fitted. Alternatively, the models for the evolution of flow stress can be implemented into crystal plasticity models. The MTS model has been implemented in crystal plasticity models to operate at the slip system level in [7,33], where the MTS is the slip resistance at 0 °K and the flow rule is an exponential function. While predictive, the model has a large number of fitting parameters. Physics-based constitutive model relying on the Orowan's equation and transition state theory with a Taylor type full-constraint homogenization has been applied to simulate constitutive behavior and microstructural evolution of Ta in [34]. Good agreement with the experiments was achieved.

The strain-rate and temperature sensitivity of metals can be well described by models that are based on thermally activated glide kinetics within crystal plasticity [35]. The activation stress for dislocation glide usually relies solely on the Schmid law. In this law, slip is activated when the stress tensor projected onto the glide plane in its glide direction reaches a value of slip resistance [36]. However, the glide in BCC metals, such as Ta, is known to violate the Schmid law. The behavior manifests in tension–compression asymmetry and plastic anisotropy [37–42]. The behavior is referred to as non-Schmid and has been attributed to the motion of the non-planar core of screw dislocations and the role that non-glide stresses play in the movement of the dislocation through the lattice [43–48]. Specifically, in addition to the Schmid tensor, there are other stress components resolved in the remaining two shear directions and the three normal components [49]. A visco-plastic self-consistent (VPSC) polycrystal model for BCC metals that includes the local non-Schmid effects has recently been developed in [50,51] and will be used in the present work.

It is desirable for rate dependence in the macroscale response to arise solely due to the rate dependence of dislocation motion on individual slip systems at the slip system level [10,52]. However, difficulty can arise from power-law, rate-sensitive, hardening law crystal visco-plasticity models [53]. The visco-plastic rate-dependent flow theory is used to uniquely determine the set of independent slip systems accommodating the imposed plastic strain [54]. The flow rule in this theory involves a power-law relation whose exponent n represents the inverse of material rate sensitivity [11,55]. Hence, the flow rule introduces undesirable rate sensitivity, which can have a marked effect on macroscale response, making it unrealistic.

The objective of this study is to develop a multi-level model that links dislocation-crystal–polycrystal-component-scale within an FE framework for simulating the rate- and temperature-sensitive deformation response of metals (where the rate sensitivity is coming solely from slip resistance) and thermally activated glide. The new formulation uses the visco-plastic flow rule at a single crystal level, with removed rate sensitivity coming from the visco-plastic power-law relation. The hardening law used is dislocation density-based [56] relying on both Schmid and non-Schmid activation stresses for dislocation glide [50]. Self-consistent method is used for homogenization and the overall procedure is formulated as implicit in hardening. Therefore, the proposed polycrystal plasticity model is a modification of the widely used VPSC model [57]. The comprehensive formulation is calibrated to simulate high strain rate- and temperature-sensitive deformation of Ta and subsequently applied to simulate a Taylor impact test of the same material. The predictions in terms of geometry and evolution of texture are compared with experiments. The implementation and results are presented and discussed in this paper.

2. Modeling framework

This section presents details of the multi-level modeling framework aimed at simulating the microstructure–property relationships in a BCC polycrystal during high strain rate and impact deformation conditions. At the macroscale, the implicit FE solver is used for solving initial boundary value problem. Local constitutive response at FE integration points is solved by self-consistent homogenization of visco-plastic polycrystal (VPSC model) [57], which integrates a dislocation density-based hardening law [58,59]. In the proposed model, the slip resistances are evolved implicitly while all the other state variables (crystal orientations, grain shape, temperature, etc.) are evolved explicitly. In addition, the macroscopic constitutive equation is also integrated implicitly.

The Taylor impact test of Ta cylinder was previously modeled in [30,34,60]. First, Bingert et al. employed a multisurface algorithm [61] to describe the yield surface of Ta obtained by Taylor–Bishop–Hill polycrystal calculations. The yield surface was only allowed to expand with the evolution of yield stress described by the MTS model [6], while the shape of the yield surface remained constant during deformation. Consequently, the texture evolution and heterogeneous hardening during deformation had no influence on the shape of the yield surface. Despite these simplifications model predicts the post-test geometry well. Subsequently, Plunkett et al. used a more sophisticated model capable of predicting effects of texture evolution and twinning on the shape of the yield surface to simulate Taylor impact tests of zirconium and tantalum cylinders [60]. In the case of zirconium cylinder, the evolution of the yield surface was predicted using the VPSC model. Next, the predicted evolution of the yield surface was fitted with the macroscopic yield criterion (CPB06). As noted before, the main drawback of this approach is that the yield surface evolution is recorded for only one specific strain history. It is clear that during Taylor impact simulation strain histories of different points are quite heterogeneous. Consequently, the predicted yield surface will deviate from the actual yield surface for points that experience strain history different from the one used during the fitting procedure. In addition, both of the modeling approaches are incapable of predicting microstructural evolution. On the other hand, Kothari and Anand proposed a sophisticated polycrystal plasticity model for simulating deformation of Ta and successfully predicted the mechanical response and microstructural evolution as a function of strain rate and temperature, including the Taylor impact tests at two different strain rates and temperatures [34]. Single crystal response was modeled using the equation of Orowan, which relates the slip system shear rates with a density of mobile dislocations and an average value of dislocation velocity [62]. The average dislocation velocity was defined in terms of the resolved shear stress, critical resolved shear stress, and temperature using the transition-state theory [63]. A homogenized response at every integration point was obtained by the full-constraint Taylor type homogenization.

In summary, the models developed by Bingert et al. and Plunkett et al. rely on fitting the yield surfaces predicted by polycrystal plasticity models. On the other hand, the model developed by Kothari and Anand as well as the model presented in this work directly uses the polycrystal plasticity constitutive law at each integration point of the finite element model facilitating more accurate predictions at a higher computational cost. As mentioned above, the work of Kothari and Anand utilized the physics-based Orowan's equation as the single crystal flow rule, while the work presented here relies on the power-law flow rule. While the former work utilized a simple empirical hardening law, the work presented here relies on a rate and temperature sensitive dislocation density-based hardening law. Moreover, the self-consistent homogenization method utilized in the present model is more advanced than the full constraint Taylor approach. In summary, we show that the widely used visco-plastic flow rule when appropriately modified, in combination with a physics-based dislocation density hardening law, can successfully predict a complex strain rate and temperature dependent response of Ta.

We begin by describing the kinematics, the single crystalline constitutive response and the hardening law (Sections 2.1–2.3). Subsequently, we describe the homogenization procedure and finite element implementation (Sections 2.4 and 2.5). In our notation, tensors will be denoted by bold letters, while scalars and tensor components will be italic and not bold. The dyadic and contracted product between two tensors will be denoted by $\otimes$ and $\cdot$, respectively.

2.1. Kinematics

In what follows we briefly describe the kinematics of a purely plastic crystal plasticity model [57,64]. Polycrystal is assumed to consist of a set of grains undergoing plastic deformation, meaning that the elasticity of the individual grains is neglected. As a result, the effective behavior of a plastic polycrystal is evaluated first. Next, the purely plastic effective medium is coupled with elasticity in an average manner [65,66], as discussed later.

Deformation gradient of grain r is given by:

$$\mathbf{F}^{(r)} = \frac{\partial \mathbf{x}}{\partial \mathbf{X}}, \tag{1}$$

where $\mathbf{x}$ and $\mathbf{X}$ are coordinates of a material point in the current and initial configurations. Velocity gradient of grain r, in the current configuration, is defined as:

$$\mathbf{L}^{(r)} = \frac{\partial \mathbf{v}}{\partial \mathbf{x}}, \tag{2}$$

where $\mathbf{v}$ is the velocity in the current configuration. Velocity gradient can be decomposed into symmetric, $\mathbf{D}^{(r)}$, and anti-symmetric, $\mathbf{W}^{(r)}$, parts. The relation between the velocity gradient and the deformation gradient is given by:

$$\dot{\mathbf{F}}^{(r)} = \mathbf{L}^{(r)}\mathbf{F}^{(r)}. \tag{3}$$

Polar decomposition allows us to decompose the total deformation gradient into pure rotation, $\mathbf{R}^{(r)}$, and plastic distortion, $\mathbf{F}_p^{(r)}$:

$$\mathbf{F}^{(r)} = \mathbf{R}^{(r)}\mathbf{F}_p^{(r)}. \tag{4}$$

The plastic distortion is assumed to shear the lattice without rotation or stretch. Next the rotation tensor rotates the lattice into final configuration. In the elasto-plastic formulation the total deformation gradient is decomposed into elastic and plastic deformation gradients. Since the elasticity is neglected the elastic deformation gradient is replaced with pure rotation. By solving Eq. (3) for velocity gradient and substituting Eq. (4) we obtain:

$$\mathbf{L}^{(r)} = \dot{\mathbf{F}}^{(r)}\mathbf{F}^{(r)^{-1}} = \dot{\mathbf{R}}^{(r)}\mathbf{R}^{(r)^{-1}} + \mathbf{R}^{(r)}\dot{\mathbf{F}}_p^{(r)}\mathbf{F}_p^{(r)^{-1}}\mathbf{R}^{(r)^{-1}}. \tag{5}$$

Term $\dot{\mathbf{R}}^{(r)}\mathbf{R}^{(r)^{-1}}$ is the lattice spin, $\mathbf{W}^{*,(r)}$, in the current configuration associated with the pure rotation. Term $\dot{\mathbf{F}}_p^{(r)}\mathbf{F}_p^{(r)^{-1}}$ is the plastic velocity gradient in the configuration before rotation, which can be expressed as superposition of slip system shear rates:

$$\mathbf{L}_p^{i,(r)} = \sum_s \dot{\gamma}^{s,(r)}\mathbf{b}^{s,i,(r)} \otimes \mathbf{n}^{s,i,(r)}, \tag{6}$$

where $\mathbf{b}^{s,i,(r)}$ and $\mathbf{n}^{s,i,(r)}$ are Burgers vector and slip plane normal in the configuration before rotation. Substituting Eq. (6) into Eq. (5) and noting that Burgers vector and slip plane normal in current configuration are given by $\mathbf{b}^{s,(r)} = \mathbf{R}^{(r)}\mathbf{b}^{s,i,(r)}$ and $\mathbf{n}^{s,(r)} = \mathbf{R}^{(r)}\mathbf{n}^{s,i,(r)}$, allows us to write the velocity gradient in current configuration as:

$$\mathbf{L}^{(r)} = \mathbf{W}^{*,(r)} + \sum_s \dot{\gamma}^{s,(r)}\mathbf{b}^{s,(r)} \otimes \mathbf{n}^{s,(r)}. \tag{7}$$

From here the symmetric part of the velocity gradient and the lattice spin are:

$$\mathbf{D}^{(r)} = \sum_s \dot{\gamma}^{s,(r)}\mathbf{m}^{s,(r)}, \tag{8}$$

$$\mathbf{W}^{*,(r)} = \mathbf{W}^{(r)} - \sum_s \dot{\gamma}^{s,(r)}\boldsymbol{\alpha}^{s,(r)}, \tag{9}$$

where $\mathbf{m}^{s,(r)}$ and $\boldsymbol{\alpha}^{s,(r)}$ are symmetric and anti-symmetric parts of Schmid tensor for slip system s calculated as $\frac{1}{2}\left(\mathbf{b}^{s,(r)} \otimes \mathbf{n}^{s,(r)} + \mathbf{n}^{s,(r)} \otimes \mathbf{b}^{s,(r)}\right)$ and $\frac{1}{2}\left(\mathbf{b}^{s,(r)} \otimes \mathbf{n}^{s,(r)} - \mathbf{n}^{s,(r)} \otimes \mathbf{b}^{s,(r)}\right)$. The lattice spin is used for incremental updating of crystallographic orientations, while the total deformation gradient within the grain is used for calculation of grain shape. In VPSC, the tensor $\mathbf{D}$ which is based on the finite kinematic structure, is replaced with a strain rate tensor, $\dot{\boldsymbol{\varepsilon}}_{vp}$, which is based on the infinitesimal kinematic structure, as will be discussed later. In the next section the relation between the instantaneous rate of deformation and stress is derived.

2.2. *Single crystal constitutive relation*

The functional relationship between the slip system shear rate, stress and the microstructural state represents the constitutive equation [67], which are either phenomenological or physically based. The former constitutive models relate the shear rate on slip system s with the resolved shear stress, τ^s, and the critical resolved shear stress of system s, τ_c^s. The first such constitutive model was the rate independent slip criterion. According to this model, once the resolved shear stress reaches the critical resolved shear stress, the slip system becomes active and the shear rate on that system can take any value:

$$\dot{\gamma}^s = 0 \text{ if } \left|\tau^s\right| < \tau_c^s, \tag{10}$$

$$\dot{\gamma}^s \neq 0 \text{ if } \left|\tau^s\right| = \tau_c^s. \tag{11}$$

The main drawback of the rate independent slip criterion is the difficulty and non-uniqueness involved in determination of active slip systems. The visco-plastic regularization of the rate independent slip criterion was introduced to alleviate those problems [11,68]:

$$\dot{\gamma}^s = \dot{\gamma}_0\left(\frac{\tau^s}{\tau_c^s}\right)^n, \tag{12}$$

where n is the inverse of rate sensitivity and $\dot{\gamma}_0$ is the reference shear rate. The visco-plastic regularization resolves the non-uniqueness issue and provides continuous functional relationship between shear rates and stress. However, it also introduces a dependence of the magnitude of shear rate on the magnitude of stress defined by the rate exponent n.

Physics-based constitutive models use the Orowan equation to relate the shear rate on slip system s with the dislocation density of mobile dislocations on slip systems s, ρ_m^s [62]:

$$\dot{\gamma}^s = \rho_m^s b^s v^s, \tag{13}$$

where b^s is the magnitude of Burgers vector and v^s is the average velocity of mobile dislocations. The dislocation density of mobile dislocations can be related to the statistically stored dislocation density through the temperature dependent scaling law [69]. The average velocity of mobile dislocations can be expressed as a complex function of resolved shear stress, critical resolved shear stress and temperature [34,67,69].

In the present model, we adopt the visco-plastic constitutive relation at the single crystal level. The visco-plastic regularization provides sufficiently accurate selection of slip system activity and continues functional relationship between stress and strain rate, which results in stable convergence properties of the overall procedure. In addition, the visco-plastic formulation with dislocation density-based hardening law has been previously successfully used for modeling of high rate deformation [56,70,71]. As will be seen in the next section, in the modified visco-plastic flow rule, the rate sensitivity is defined solely through the rate dependence of slip resistance, while the rate exponent n only determines the accuracy of slip system selection. Therefore, the slip system selection is not influenced by the material rate sensitivity. The Orowan equation approach [34] couples the slip system selection and rate sensitivity and, as a result, the increase in the rate sensitivity causes damping in the relation between shear rate and resolved shear stress, which is similar to reducing the rate exponent n in Eq. (12). Since the rate sensitivity increases with temperature at higher rates, the damping effect increases as well. As a result, it is possible to have shifts in active slip systems with increase of temperature, which cannot happen in simulations using the modified power-law flow rule, where the slip system selection and rate sensitivity are separated. In the modified visco-plastic flow rule, the slip system activation is determined solely by a constant rate exponent, while the slip resistances scale with strain rate and temperature and, in turn, determine the rate sensitivity. Physically, at elevated temperature, the Peierls barrier decreases equally for all slip systems and the activity of slip systems is not expected to change from that at lower temperature, unless different slip modes activate. Finally, it is important to describe advances in the visco-plastic flow rule formulation since a large number of model developments relying on it can take the advantage of any new advances. In the next section, consequences of the adopted visco-plastic flow rule on the rate sensitivity and the necessary modifications to the flow rule are discussed. Subsequently, the functional relationship between the resolved shear stress and the applied stress is derived for the case of BCC Ta.

2.2.1. Accurate representation of strain rate sensitivity with visco-plastic power-law flow rule

Follansbee and Kocks define two rate effects within polycrystalline materials [29]. The first rate effect is the rate sensitivity of stress at constant structure (dislocation density). For FCC materials this rate effect is fairly small [29]. On the other hand, in BCC materials very high rate sensitivity at constant structure and low temperatures is observed and attributed to rate dependence of Peierls barrier [6,72]. At elevated temperatures the rate sensitivity of BCC materials diminishes. The second rate effect is the rate dependence of structure evolution. Essentially, the rate of dislocation accumulation depends on the rate at which deformation happens [29,56]. Both of these rate effects influence the macroscopic stress only through the resistance to slip. The rate sensitivity of the material at constant structure, m, is thus defined as:

$$m = \frac{\partial \ln |\boldsymbol{\sigma}|}{\partial \ln |\dot{\boldsymbol{\varepsilon}}|} = \sum_r \sum_s \frac{\partial \ln |\boldsymbol{\sigma}|}{\partial \tau_c^{s,(r)}} \frac{\partial \tau_c^{s,(r)}}{\partial \ln |\dot{\boldsymbol{\varepsilon}}|} \left(\rho^{(r)} = \text{const}\right), \tag{14}$$

where $\rho^{(r)}$ is total dislocation density within the grain r. Therefore, it is physical and thus desirable to describe the rate sensitivity of the material solely through the rate dependence of slip resistance and its evolution.

The adopted visco-plastic flow rule with the rate sensitive slip resistance displays a serious issue. The visco-plastic constitutive relation at the grain level (Eq. (12)) introduces an additional, artificial and unphysical rate sensitivity of the stress at constant structure. This rate sensitivity is an undesirable consequence of the adopted power-law flow

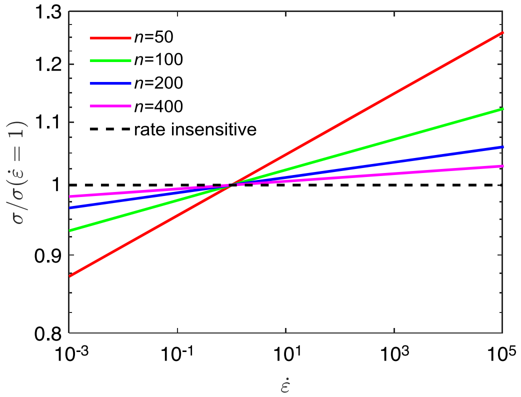

Fig. 1. Effect of the power-law exponent n on the mechanical response in simple compression as a function of imposed strain rate.

rule used for the slip system selection. Consequently, the expression for the rate sensitivity of the material at constant structure contains an additional term arising due to the power-law flow rule:

$$m=\frac{\partial\ln|\boldsymbol{\sigma}|}{\partial\ln|\dot{\boldsymbol{\varepsilon}}|}=\underbrace{\frac{\partial\ln|\boldsymbol{\sigma}|}{\partial\ln|\dot{\boldsymbol{\varepsilon}}|}\left(\tau_c^{s,(r)}=\text{const}\right)}_{1/n}+\sum_r\sum_s\frac{\partial\ln|\boldsymbol{\sigma}|}{\partial\tau_c^{s,(r)}}\frac{\partial\tau_c^{s,(r)}}{\partial\ln|\dot{\boldsymbol{\varepsilon}}|}\left(\rho^{(r)}=\text{const}\right). \tag{15}$$

Next, we consider two methods for removal of the artificially introduced rate sensitivity caused by the power-law flow rule [33,73]: increase of rate exponent n and rate insensitive approach.

The rate sensitivity arising due to the adopted power-law relation at slip system level is inversely proportional to the rate exponent n. Therefore, increase of rate exponent n results in decrease of rate sensitivity and the limiting case when n goes to infinity ($n\rightarrow\infty$) results in a rate-insensitive response. However, with the increase of rate exponent n the visco-plastic equation becomes very stiff and difficult to solve. Numerical considerations limit the rate exponent to values $n\leq 100$ [11,55,74]. Consequently, the rate sensitivity due to the power-law flow rule cannot be completely removed using this method. Considering that strain rates during the Taylor impact vary over several orders of magnitude the retained rate sensitivity when $n=100$ is unacceptable. Fig. 1 shows the rate dependence of stress over a wide range of strain rates for different values of rate exponent. The magnitude of stress is normalized by the stress magnitude at reference strain rate of 1.0 s^{-1}. Fig. 1 indicates that the rate exponent in the range $n\leq 400$ results in artificial rate sensitivity affecting the stress. The effect is enhanced with the magnitude of applied strain rate.

In the second method, the reference shear rate, $\dot{\gamma}_0$, is set to the norm of the applied macroscopic strain rate, $\dot{\varepsilon}=\left|\dot{\boldsymbol{\varepsilon}}_{vp}\right|=\left|\left\langle\dot{\boldsymbol{\varepsilon}}_{vp}^{(r)}\right\rangle\right|$, where $\langle\,\rangle$ denotes volume average over all grains. By moving the reference shear rate to the left side of the expression for strain rate we get:

$$\dot{\boldsymbol{\varepsilon}}_{vp}^{(r)}/\left|\left\langle\dot{\boldsymbol{\varepsilon}}_{vp}^{(r)}\right\rangle\right|=\sum_s\left(\frac{\tau^{s,(r)}}{\tau_c^{s,(r)}}\right)^n\mathbf{m}^{s,(r)}. \tag{16}$$

The grain strain rate is thus normalized with the macroscopic strain rate magnitude. The magnitude of the grain stress is then affected only by the ratio of the grain strain rate magnitude and the macroscopic strain rate magnitude. Since the deviation of grain strain rates from the macroscopic strain rate is not large in BCC polycrystals, this effect on grain stress is fairly small. Consequently the effect of the grain strain rate magnitude on the grain stress is minimized and the direction of grain strain rate determines both the magnitude and the direction of the grain stress. Macroscopically, the rate sensitivity of stress due to the power-law flow rule is completely removed and magnitude of the applied strain rate has absolutely no effect on the macroscopic stress magnitude or direction. The rate insensitive approach has been used in numerous studies to effectively remove the artificial rate sensitivity of macroscopic stress due to the power-law flow rule [33,56,75–80]. In the present study we adopt the rate insensitive approach for removal of unphysical rate sensitivity arising due to the power-law flow rule.

The expression for the rate sensitivity of the polycrystal with the rate insensitive visco-plastic flow rule is given by Eq. (14). Let us consider the effect of the integration procedure for the slip resistances on the material rate sensitivity in the context of implicit finite elements. In a large number of implicit finite element crystal plasticity codes the slip resistances and other state variables are held constant while the stress state is calculated implicitly [65,67,81–83]. Next the state variables are updated explicitly. Consequently, the expression for the slip resistance at the current time increment is defined solely in terms of the quantities from the previous time increment. As a result of the adopted integration procedure, the slip resistance at the current increment is independent on the currently applied visco-plastic strain rate. Consequently, the derivatives of slip resistance with the strain rate vanish, $\frac{\partial \tau_c^{s,(r)}}{\partial \ln|\dot{\boldsymbol{\varepsilon}}|} = 0$, and the material behaves as completely rate insensitive regardless of the functional relation between the slip resistance and strain rate. The explicit integration of hardening variables would be suitable if used within an explicit finite element formulation. In implicit finite elements, the expression for slip resistance should be a function of the currently applied strain rate. While an improved explicit method, in which the slip resistances are first updated using the current strain rate and strain increment and subsequently used for the calculation of stress, would suffice, we adopt an implicit method for the evolution of slip resistances. The implicit integration of the slip resistances results in the most accurate solution. Shears at each slip system are integrated using an implicit Euler backward method, while the slip resistances are integrated as function of the shear using an implicit Crank–Nicolson method [84]. The slip resistance at the current increment is thus defined based on the quantities from the current increment. Any change of the currently applied strain rate will result in the change of the slip resistance and thus the stress. Therefore, the rate sensitivity of stress at constant structure is solely defined through the rate dependence of the slip resistance which is the desired behavior. Also, note that the rate sensitivity of the stress due to rate sensitive structure evolution will be captured as well: $\sum_r \sum_s \sum_{s'} \frac{\partial \ln|\boldsymbol{\sigma}|}{\partial \tau_c^{s,(r)}} \frac{\partial \tau_c^{s,(r)}}{\partial \rho^{s',(r)}} \frac{\partial \rho^{s',(r)}}{\partial \ln|\dot{\boldsymbol{\varepsilon}}|}$.

In summary, in the adopted rate insensitive power-law flow rule with implicit integration of slip resistances, the rate sensitivity is defined by the functional relationship between slip resistance and strain rate. The rate exponent, n, does not affect the rate sensitivity and only determines the accuracy of the slip system selection.

2.2.2. Non-Schmid activation

Slip resistance, $\tau_c^{s,(r)}$, in Eq. (12) physically represents the resistance to motion of dislocation on slip system s while the stress projection in Eq. (12), $\tau^{s,(r)} = \mathbf{m}^{s,(r)} \cdot \boldsymbol{\sigma}'^{(r)}$, represents the shear stress in the dislocation glide plane and in the direction of slip. According to the Schmid law, the system becomes active when resolved shear stress reaches or exceeds the resistance of the dislocation motion [36]. However, the glide in BCC metals is known to violate the Schmid law. The non-Schmid effects on the dislocation motion are introduced by adding the contribution of the non-Schmid stress projections to the Schmid resolved shear stress [45,49,50,85]:

$$\tau^{s,(r)} = \mathbf{m}^{s,(r)} \cdot \boldsymbol{\sigma}'^{(r)} + \mathbf{m}_{nS}^{s,(r)} \cdot \boldsymbol{\sigma}'^{(r)} = \mathbf{m}_{tot}^{s,(r)} \cdot \boldsymbol{\sigma}'^{(r)}, \tag{17}$$

where $\mathbf{m}_{tot}^{s,(r)} = \mathbf{m}^{s,(r)} + \mathbf{m}_{nS}^{s,(r)}$ and $\mathbf{m}_{nS}^{s,(r)}$ represents a non-Schmid tensor given as weighted sum of the following dyads:

$$\mathbf{m}_{nS}^{s,(r)} = c_1 \left(\mathbf{t}^s \otimes \mathbf{b}^s\right) + c_2 \left(\mathbf{t}^s \otimes \mathbf{n}^s\right) + c_3 \left(\mathbf{n}^s \otimes \mathbf{n}^s\right) + c_4 \left(\mathbf{t}^s \otimes \mathbf{t}^s\right) - (c_3 + c_4) \left(\mathbf{b}^s \otimes \mathbf{b}^s\right), \tag{18}$$

where $\mathbf{t}^s$ is unit vector in the glide plane perpendicular to the slip direction, $\mathbf{t}^s = \mathbf{n}^s \times \mathbf{b}^s$ and c_i are non-Schmid coefficients. The coefficients, c_i, for Ta at room temperature reported in [45] are used: $c_1 = -0.15, c_2 = 0.13, c_3 = -0.07, c_4 = 0.04$.

The non-Schmid effects are a complicated function of strain, strain rate and temperature [45,86–88]. However, in the present study, we assume that the non-Schmid effects do not vary with strain rate due to lack of reliable experimental data in literature. An expression for non-Schmid tensor as a function of temperature and strain is given by [86,88]:

$$\begin{aligned} \mathbf{m}_{nS}^{s,(r)}\left(T, \varepsilon_{eq}\right) = \exp\left(-\frac{\varepsilon_{eq}}{\varepsilon_0}\right) \Bigg\{ & c_1 \left(\mathbf{t}^s \otimes \mathbf{b}^s\right) + \left(1 - \frac{T - 300}{T_c - 300}\right) \frac{\operatorname{sgn}\left(T_c - T\right) + 1}{2} \Big[c_2 \left(\mathbf{t}^s \otimes \mathbf{n}^s\right) \\ & + c_3 \left(\mathbf{n}^s \otimes \mathbf{n}^s\right) + c_4 \left(\mathbf{t}^s \otimes \mathbf{t}^s\right) - (c_3 + c_4) \left(\mathbf{b}^s \otimes \mathbf{b}^s\right) \Big] \Bigg\}, \end{aligned} \tag{19}$$

where ε_0 is a fitting constant and T_c is a temperature at which non-Schmid effects vanish. For simplicity, the same Eq. (19) is assumed to hold for both $\{1\bar{1}0\}\langle 111\rangle$ and $\{11\bar{2}\}\langle 111\rangle$ slip modes, although much more is known (by MD work) for the 110 systems. Temperature and strain dependence of non-Schmid effects given by Eq. (19) is an approximation based on the modeling efforts of other authors. We have conducted a detailed study of the effects of the fitting parameters in Eq. (19) on results. It was observed that strong presence of non-Schmid effects leads to unreasonable texture predictions at higher strains indicating that their effect likely quickly diminishes with strain which is in agreement with [86]. With straining of a crystal, dislocations accumulate and dislocation–dislocation interactions diminish the effect of non-Schmid stresses [86]. The constant ε_0 determining the rate at which non-Schmid effects decay with strain was thus set to 0.07. The temperature at which non-Schmid effects vanish, T_c, was approximated as 700 K for Ta [88]. The decay of non-Schmid effects with temperature was approximated as linear. The chosen values for the fitting parameters in Eq. (19) are quite conservative, limiting the influence of the non-Schmid effects only to small strains where the non-Schmid effects are experimentally observed and measured.

2.3. Dislocation density-based hardening law

Hardening law defines the slip resistance and its evolution as a function of strain rate, temperature and accumulated shear. Phenomenological hardening laws are still predominantly used in crystal plasticity models [67,89–91]. However, in the past decades several dislocation density-based hardening laws have been developed and successfully used for constitutive modeling of materials at different strain rates and temperatures. We adopt dislocation density-based hardening law developed by Beyerlein and Tome [56], which was previously used numerous times for modeling of constitutive behavior at high rates and temperatures. In what follows, the quantities from the start of the time increment will be explicitly denoted with superscript t, while all the other variables will be understood to be at the end of the time increment. The slip resistance of slip mode α is defined as [56]:

$$\tau_c^\alpha = \tau_0^\alpha + \tau_{for}^\alpha \left(\rho_{for}^\alpha\right) + \tau_{deb}^\alpha \left(\rho_{deb}\right). \tag{20}$$

where τ_0^α is an initial value of slip resistance, τ_{for}^α is a contribution to the slip resistance due to accumulation of forest dislocations, ρ_{for}^α, and τ_{deb}^α is a contribution to the slip resistance due to accumulation of debris dislocations, ρ_{deb}. The initial slip resistance, τ_0^α, represents resistance to intrinsic barriers (such as the Peierls stress), and it is dependent on strain rate and temperature [70–72,92]. We use the following empirical function to model the dependence (no summation over repeated indices):

$$\tau_0^\alpha = G^\alpha + A^\alpha \exp\left(-\frac{T^t}{B^\alpha}\right)\left(\frac{\dot{\varepsilon}}{\dot{\varepsilon}_{ref}}\right)^{C^\alpha}, \tag{21}$$

where A^α, B^α, C^α, and G^α are constants, $\dot{\varepsilon} = \sqrt{2/3}\left|\dot{\boldsymbol{\varepsilon}}_{vp}\right|$ is macroscopic equivalent plastic strain rate, and T^t is temperature. $\dot{\varepsilon}_{ref} = 1\ \mathrm{s}^{-1}$ is a reference strain rate, which normalizes the applied strain rate and makes the quantity raised to power dimensionless. As the temperature increases and the strain rate decreases, τ_0^α conveniently approaches the value of G^α for high temperature deformation under quasi-static conditions. Exponential decay of initial slip resistance with temperature is often reported in literature [50,56,70]. The power law dependence of initial slip resistance with strain rate provides the best fit to the initial yield stresses. The initial slip resistance does not evolve with strain.

The force required to move a dislocation increases with the increase of the dislocation density within the grain because the dislocations which intersect the slip plane of gliding dislocation act as barriers for the dislocation motion. The forest and debris contributions to slip resistance, dependent on forest (ρ_{for}^α) and debris (ρ_{deb}) dislocation densities, are given by (no summation over repeated indices):

$$\tau_{for}^\alpha = b^\alpha \mu \sqrt{\sum_{\alpha'} \chi^{\alpha\alpha'} \rho_{for}^{\alpha'}}, \tag{22}$$

$$\tau_{deb}^\alpha = -k_{deb} \mu b^\alpha \sqrt{\rho_{deb}} \log\left(b^\alpha \sqrt{\rho_{deb}}\right), \tag{23}$$

where b^α is the Burgers vector of mode α (which is 2.8579×10^{-10} m), $\chi^{\alpha\alpha'}$ is the interaction between mode α and α', and k_{deb} is a material-independent constant determined to be 0.086, which ensures that the extended law Eq. (23) converges to the conventional law (i.e. Eq. (22)) when ρ_{deb} is sufficiently small. The interaction matrix is $0.9,\ \text{if}\ \alpha = \alpha'$ and $0,\ \text{if}\ \alpha \neq \alpha'$. Shear modulus, μ, is assumed to be a function of temperature [72]:

$$\mu\left(T^t\right) = \mu_0 - \frac{D}{\exp\left(\frac{T_0}{T^t}\right) - 1}, \tag{24}$$

with $\mu_0 = 65\,250$ MPa, $D = 380$ MPa, and $T_0 = 40$ K. Resistance to the short range obstacles (forest dislocations) was observed to be rate sensitive [29,72]. However, considering that this dependence is fairly weak, it was neglected [56].

During deformation, the dislocation generation mechanisms increase the density of the forest dislocations while the temperature and rate sensitive dislocation removal mechanisms reduce it. As a result, the forest dislocation density quickly increases with strain and saturates at higher strains. A fraction of the removed dislocations become debris dislocations. The forest and debris dislocation densities are evolved with shear using the implicit Crank–Nicolson method [84] (no summation over repeated indices):

$$\rho^{\alpha}_{for} = \rho^{\alpha,t}_{for} + \frac{1}{2}\left[\frac{\partial \rho^{\alpha}_{for}}{\partial \gamma^{\alpha}}\left(\rho^{\alpha,t}_{for}\right) + \frac{\partial \rho^{\alpha}_{for}}{\partial \gamma^{\alpha}}\left(\rho^{\alpha}_{for}\right)\right]\sum_{s(\alpha)}\left|\dot{\gamma}^{s}\right|\Delta t, \tag{25}$$

$$\rho_{deb} = \rho^{t}_{deb} + \sqrt{\rho_{deb}}\sum_{\alpha}\left\{q^{\alpha}b^{\alpha}\frac{1}{2}\left[\frac{\partial \rho^{\alpha}_{rem,for}}{\partial \gamma^{\alpha}}\left(\rho^{\alpha,t}_{for}\right) + \frac{\partial \rho^{\alpha}_{rem,for}}{\partial \gamma^{\alpha}}\left(\rho^{\alpha}_{for}\right)\right]\sum_{s(\alpha)}\left|\dot{\gamma}^{s}\right|\Delta t\right\}, \tag{26}$$

where $s(\alpha)$ denotes a set of slip systems within slip mode α. The increments in shears on slip systems are calculated using the implicit Euler backward method. The rate of change of forest dislocations with shear strain on mode α is given by (no summation over repeated indices):

$$\frac{\partial \rho^{\alpha}_{for}}{\partial \gamma^{\alpha}} = \frac{\partial \rho^{\alpha}_{gen,for}}{\partial \gamma^{\alpha}} - \frac{\partial \rho^{\alpha}_{rem,for}}{\partial \gamma^{\alpha}} = k^{\alpha}_{1}\sqrt{\rho^{\alpha}_{for}} - k^{\alpha}_{2}\left(\dot{\varepsilon}, T^{t}\right)\rho^{\alpha}_{for}. \tag{27}$$

The coefficient k^{α}_{1} accounts for dislocation storage, while rate and temperature sensitive coefficient k^{α}_{2} accounts for the dislocation removal through thermally activated mechanisms and is given by (no summation over repeated indices):

$$k^{\alpha}_{2} = \frac{k^{\alpha}_{1}}{\sqrt{\sum_{\alpha'}\left(\chi^{-1}\right)^{\alpha\alpha'}\left(\frac{\tau^{\alpha'}_{sat}}{b^{\alpha'}\mu}\right)^{2}}};\ \tau^{\alpha'}_{sat} = \frac{D^{\alpha}\left(b^{\alpha}\right)^{3}g^{\alpha}\mu}{D^{\alpha}\left(b^{\alpha}\right)^{3} - kT^{t}\log\left(\frac{\dot{\varepsilon}}{\dot{\varepsilon}_0}\right)}, \tag{28}$$

where D^{α} is drag stress, g^{α} is the effective activation enthalpy, k is Boltzmann constant, and $\dot{\varepsilon}_0$ is the reference strain rate (taken to be $10^{7}\ \mathrm{s}^{-1}$) [56].

At constant structure, the rate and temperature sensitivity is defined by the resistance to intrinsic barriers, τ^{α}_{0}. During straining, the accumulation of dislocations reduces the relative contribution of τ^{α}_{0} to total slip resistance, τ^{α}_{c}. Consequently, the rate and temperature sensitivity will change during straining. Since the evolution of dislocation densities is strain rate and temperature dependent, attempting to capture the complicated strain rate sensitivity of metals such as Ta using the power-law exponent n (or m) would be inappropriate. Therefore, we aim at using the power-law, rate-insensitive visco-plastic flow rule in combination with the rate and temperature sensitive dislocation density-based hardening law, along with the initial slip resistance to describe the strain rate and temperature sensitive deformation of Ta. As a result, dislocation glide while the structure is evolving governs the material behavior. The next section presents homogenization procedure of the visco-plastic polycrystal with the implicit integration of slip resistances.

2.4. Self-consistent homogenization of visco-plastic polycrystal

Homogenization procedure links the response of the constituent grains to the macroscopic response of the polycrystal. Taylor full-constraint, self-consistent and grain cluster homogenization schemes are most frequently used in the polycrystal plasticity models [67]. In the present model, the self-consistent homogenization method is used. In what follows, the self-consistent homogenization of the visco-plastic polycrystal proposed by Lebensohn and Tome is presented along with the necessary modifications for implicit slip resistance evolution [57]. The non-linear constitutive relation at the grain level is given by the visco-plastic equation with non-Schmid activation:

$$\dot{\boldsymbol{\varepsilon}}^{(r)}_{vp} = \dot{\gamma}_0\sum_{\alpha}\left\{\sum_{s(\alpha)}\left(\frac{\mathbf{m}^{s,t,(r)}_{tot}\cdot\boldsymbol{\sigma}'^{(r)}}{\tau^{\alpha,(r)}_{c}}\right)^{n}\mathbf{m}^{s,t,(r)}\right\}. \tag{29}$$

The rate exponent is set to $n = 20$. This value allows accurate selection of slip systems. Increasing the value of n does not change the results predicted by the rate insensitive visco-plastic flow rule in any appreciable way. Note that $\tau_c^{\alpha,(r)}$ is calculated at the end of the time increment, $t + \Delta t$, using the implicit integration rule. The increments in shear are calculated using the Euler backward method while the slip resistance is integrated as a function of the shear using the implicit Crank–Nicolson method [84]. Hence, $\tau_c^{\alpha,(r)}$ is a function of $\left|\dot{\gamma}^{s,(r)}\right|$, where the exact functional relationship is defined by the adopted hardening law. The linearized form of the constitutive relation at the grain level is:

$$\dot{\boldsymbol{\varepsilon}}_{vp}^{(r)} = \mathbf{M}^{(r)}\boldsymbol{\sigma}'^{(r)} + \dot{\boldsymbol{\varepsilon}}_{vp}^{0,(r)}, \tag{30}$$

where $\mathbf{M}^{(r)}$ and $\dot{\boldsymbol{\varepsilon}}_{vp}^{0,(r)}$ are visco-plastic compliance and back extrapolated strain rate [93]. For the affine linearization, the derivation of $\mathbf{M}^{(r)}$ and $\dot{\boldsymbol{\varepsilon}}_{vp}^{0,(r)}$ in the case of implicit hardening is given next.

First, it should be noted that slip resistance, $\tau_c^{\alpha,(r)}$, represents a function of deviatoric stress, defined by the hardening law, through the shear rates, which are functions of deviatoric stress. Next we introduce a function, **f**, that maps deviatoric stress directly to visco-plastic strain rate:

$$\dot{\boldsymbol{\varepsilon}}_{vp}^{(r)}\left(\boldsymbol{\sigma}'^{(r)}, \tau_c^{\alpha,(r)}\left(\boldsymbol{\sigma}'^{(r)}\right)\right) = \mathbf{f}\left(\boldsymbol{\sigma}'^{(r)}\right). \tag{31}$$

Taylor expansion of strain rate around reference stress value, $\boldsymbol{\sigma}_0^{\prime,(r)}$, is then given by:

$$\dot{\boldsymbol{\varepsilon}}_{vp}^{lin,(r)}\left(\boldsymbol{\sigma}'^{(r)}\right) = \mathbf{f}\left(\boldsymbol{\sigma}_0'^{(r)}\right) + \left.\frac{\partial \mathbf{f}}{\partial \boldsymbol{\sigma}'^{(r)}}\right|_{\boldsymbol{\sigma}_0'^{(r)}}\left(\boldsymbol{\sigma}'^{(r)} - \boldsymbol{\sigma}_0'^{(r)}\right). \tag{32}$$

Then the grain compliance and back-extrapolated strain rate are:

$$\mathbf{M}^{(r)} = \left.\frac{\partial \mathbf{f}}{\partial \boldsymbol{\sigma}'^{(r)}}\right|_{\boldsymbol{\sigma}_0'^{(r)}}, \tag{33}$$

$$\dot{\boldsymbol{\varepsilon}}_{vp}^{0,(r)} = \mathbf{f}\left(\boldsymbol{\sigma}_0'^{(r)}\right) - \left.\frac{\partial \mathbf{f}}{\partial \boldsymbol{\sigma}'^{(r)}}\right|_{\boldsymbol{\sigma}_0'^{(r)}}\boldsymbol{\sigma}_0'^{(r)}. \tag{34}$$

The derivatives of the function, **f**, w.r.t. deviatoric stress are given by:

$$\mathbf{M}^{(r)} = \frac{\partial \mathbf{f}}{\partial \boldsymbol{\sigma}'^{(r)}} = \underbrace{\frac{\partial \dot{\boldsymbol{\varepsilon}}_{vp}^{(r)}}{\partial \boldsymbol{\sigma}'^{(r)}}}_{\text{Term (1)}} + \underbrace{\frac{\partial \dot{\boldsymbol{\varepsilon}}_{vp}^{(r)}}{\partial \tau_c^{\alpha,(r)}}}_{\text{Term (2)}}\underbrace{\frac{\partial \tau_c^{\alpha,(r)}}{\partial \boldsymbol{\sigma}'^{(r)}}}_{\text{Term (3)}}. \tag{35}$$

The individual terms are provided in the Appendix.

The macroscopic response of the homogenized linear polycrystal will also be linear:

$$\dot{\boldsymbol{\varepsilon}}_{vp} = \mathbf{M}\boldsymbol{\sigma}' + \dot{\boldsymbol{\varepsilon}}_{vp}^{0}, \tag{36}$$

where $\mathbf{M}$ and $\dot{\boldsymbol{\varepsilon}}_{vp}^{0}$ are macroscopic visco-plastic compliance and back extrapolated strain rate. In the case of self-consistent homogenization, every grain is treated as an ellipsoidal inhomogeneity within the effective medium, which has the properties of macroscopic homogenized polycrystal. The interaction law is given by [57,94]:

$$\tilde{\dot{\boldsymbol{\varepsilon}}}_{vp}^{(r)} = -\widetilde{\mathbf{M}}\tilde{\boldsymbol{\sigma}}'^{(r)}, \tag{37}$$

where $\tilde{\dot{\boldsymbol{\varepsilon}}}_{vp}^{(r)}$ and $\tilde{\boldsymbol{\sigma}}'^{(r)}$ are strain rate and stress deviations with respect to macroscopic strain rate and stress, and $\widetilde{\mathbf{M}}$ is interaction tensor calculated as:

$$\widetilde{\mathbf{M}} = (\mathbf{I} - \mathbf{S})^{-1}\mathbf{S}\mathbf{M}, \tag{38}$$

where **S** is the Eshelby tensor. The macroscopic moduli are calculated as:

$$\mathbf{M} = \left\langle \mathbf{M}^{(r)}\mathbf{B}^{(r)} \right\rangle, \tag{39}$$

$$\dot{\boldsymbol{\varepsilon}}_{vp}^{0} = \left\langle \mathbf{M}^{(r)}\mathbf{b}^{(r)} + \dot{\boldsymbol{\varepsilon}}_{vp}^{0,(r)} \right\rangle, \tag{40}$$

Table 1
Numerical procedure for the implicit hardening in VPSC — outer iterative loop for solving for stress in grains.

(1)	Solve the self-consistent equations and calculate macroscopic compliance and back-extrapolated strain rate: $\mathbf{M}^{i} = \langle \mathbf{M}^{(r),i} \mathbf{B}^{(r),i} \rangle$ $\dot{\boldsymbol{\varepsilon}}_{vp}^{0,i} = \left\langle \mathbf{M}^{(r),i} \mathbf{b}^{(r),i} + \dot{\boldsymbol{\varepsilon}}_{vp}^{0,(r),i} \right\rangle$
(2)	Calculate macroscopic stress, $\boldsymbol{\sigma}'^{i}$, from the applied strain rate: $\boldsymbol{\sigma}'^{i} = {\mathbf{M}^{i}}^{-1} \left(\dot{\boldsymbol{\varepsilon}}_{vp} - \dot{\boldsymbol{\varepsilon}}_{vp}^{0,i} \right)$
(3)	Solve the interaction equation for each grain and obtain a new guess for grain stresses, $\boldsymbol{\sigma}'^{(r),i+1}$: $\dot{\boldsymbol{\varepsilon}}_{vp} - \dot{\gamma}_0 \sum_s \left(\frac{\mathbf{m}_{tot}^{s,t,(r)} \cdot \boldsymbol{\sigma}'^{(r),i+1}}{\tau_c^{\alpha,(r),i+1}} \right)^n \mathbf{m}^{s,t,(r)} = -\widetilde{\mathbf{M}}^{i} \left(\boldsymbol{\sigma}'^{i} - \boldsymbol{\sigma}'^{(r),i+1} \right)$ where slip resistance at the end of the time increment is also a function of the stress: $\tau_c^{\alpha,(r),i+1} = g \left(\left\lvert \dot{\gamma}^{s} \left(\boldsymbol{\sigma}'^{(r),i+1}, \tau_c^{\alpha,(r),i+1} \left(\boldsymbol{\sigma}'^{(r),i+1} \right) \right) \right\rvert \right).$
(4)	Calculate the grain compliances, $\mathbf{M}^{(r),i+1}$, and back-extrapolated strain rates, $\dot{\boldsymbol{\varepsilon}}_{vp}^{0(r),i+1}$.
(5)	Test for convergence: **if** $\left(\frac{\sqrt{\sum_r \sum_k \left(\sigma_k'^{(r),i+1} - \sigma_k'^{(r),i} \right)^2 w^{(r)}}}{\lvert \boldsymbol{\sigma}'^{i} \rvert} < \mathrm{tol} \right)$ **and** $\left(\frac{\left\lvert \boldsymbol{\sigma}'^{i} - \left\langle \boldsymbol{\sigma}'^{(r),i+1} \right\rangle \right\rvert}{\frac{1}{2} \lvert \boldsymbol{\sigma}'^{i} + \langle \boldsymbol{\sigma}'^{(r),i+1} \rangle \rvert} < \mathrm{tol} \right)$ **and** $\left(\frac{\left\lvert \dot{\boldsymbol{\varepsilon}}_{vp} - \left\langle \dot{\boldsymbol{\varepsilon}}_{vp}^{(r),i+1} \right\rangle \right\rvert}{\frac{1}{2} \left\lvert \dot{\boldsymbol{\varepsilon}}_{vp} + \left\langle \dot{\boldsymbol{\varepsilon}}_{vp}^{(r),i+1} \right\rangle \right\rvert} < \mathrm{tol} \right)$**: exit** **else: go to** (1)

where $\mathbf{B}^{(r)}$ and $\mathbf{b}^{(r)}$ are stress localization tensors given by [57]:

$$\mathbf{B}^{(r)} = \left(\mathbf{M}^{(r)} + \widetilde{\mathbf{M}} \right)^{-1} \left(\mathbf{M} + \widetilde{\mathbf{M}} \right), \tag{41}$$

$$\mathbf{b}^{(r)} = \left(\mathbf{M}^{(r)} + \widetilde{\mathbf{M}} \right)^{-1} \left(\dot{\boldsymbol{\varepsilon}}_{vp}^{0} - \dot{\boldsymbol{\varepsilon}}_{vp}^{0,(r)} \right). \tag{42}$$

The lattice spin is given by:

$$\mathbf{W}^{*(r)} = \mathbf{W} + \boldsymbol{\Pi}^{(r)} - \mathbf{W}^{p,(r)}, \tag{43}$$

where $\mathbf{W}$ is the macroscopic spin, $\boldsymbol{\Pi}^{(r)}$ is the spin associated with the ellipsoidal inclusion and $\mathbf{W}^{p,(r)}$ is the plastic spin calculated as:

$$\mathbf{W}^{p,(r)} = \sum_{s} \dot{\gamma}^{s,(r)} \boldsymbol{\alpha}^{s,t,(r)}. \tag{44}$$

The equations are solved numerically by adjusting the grain stresses, $\boldsymbol{\sigma}'^{(r)}$, iteratively using a fixed point method [57]. The procedure starts with the initial guess for grain stresses, $\boldsymbol{\sigma}'^{(r),0}$, obtained using a full constraint (Taylor) approximation ($\dot{\boldsymbol{\varepsilon}}_{vp}^{(r),0} = \dot{\boldsymbol{\varepsilon}}_{vp}$). Subsequently, grain compliances, $\mathbf{M}^{(r),0}$, and back-extrapolated strain rates, $\dot{\boldsymbol{\varepsilon}}_{vp}^{0,(r),0}$, can be calculated based on the initial guess for stress, $\boldsymbol{\sigma}'^{(r),0}$. The last superscript on the right denotes the iteration number within the loop over grain stresses (0 for initial guess). Table 1 summarizes the procedure for the calculation of new guess for grain stresses ($\boldsymbol{\sigma}'^{(r),i+1}$) from the previous guess ($\boldsymbol{\sigma}'^{(r),i}$). The algorithm iteratively corrects the grain stresses until the convergence is reached. The tolerances for the convergence of grain stresses, tol, appearing in Table 1 are set to 0.001.

From the numerical procedure outlined in Table 1, it follows that for each iteration, i, of the outer loop over the grain stresses, the interaction equation (step 3 in Table 1) has to be solved numerically. In the case of explicit hardening, the interaction equation is simply solved for the grain stress using a Newton's method. On the other hand, in the case of implicit hardening the slip resistance becomes a function of the grain stress through the shear rates and the hardening law. We have found that a two level numerical procedure is the most stable and computationally efficient approach. The slip resistances, $\tau_c^{\alpha,(r)}$, are iteratively adjusted using a fixed point method. During each iteration over slip resistances the interaction equation has to be solved for stress using the Newton's method. The initial guess for the slip resistances is the value from a previous iteration of the outer loop for grain stresses, ${}^{0}\tau_c^{\alpha,(r),i}$. Here, the superscript on the left side denotes the iteration within the inner loop over slip resistances, while superscript on the right side denotes the outer iteration loop over grain stresses. Table 2 outlines the procedure for the calculation of new guess for slip resistance, ${}^{j+1}\tau_c^{\alpha,(r),i+1}$, based on the previous guess, ${}^{j}\tau_c^{\alpha,(r),i+1}$. The tolerance for convergence of slip resistances, tol, in Table 2 is set to 0.0005.

2.5. Finite element implementation of VPSC implicit in hardening

The implementation of VPSC within implicit finite elements code ABAQUS STANDARD termed FE-VPSC follows the approach presented in [82]. At each integration point of the FE model, the stress rate in global frame, $\dot{\boldsymbol{\sigma}}$, is given by [11,95]:

$$\dot{\boldsymbol{\sigma}} = \left\langle \dot{\boldsymbol{\sigma}}^{(r)} \right\rangle = \left\langle \mathbf{C}^{(r)} \dot{\boldsymbol{\varepsilon}}_{el}^{(r)} \right\rangle + \left\langle \mathbf{W}^{*(r)} \boldsymbol{\sigma}^{(r)} - \boldsymbol{\sigma}^{(r)} \mathbf{W}^{*(r)} \right\rangle, \tag{45}$$

where $\mathbf{C}^{(r)}$ is elastic stiffness of a grain r and $\dot{\boldsymbol{\varepsilon}}_{el}^{(r)}$ is the elastic strain rate within the grain r. The single crystal elastic constants for Ta are taken as $C_{11} = 267$ GPa, $C_{12} = 161$ GPa and $C_{44} = 82.5$ GPa. After the integration of the constitutive equation and decoupling of elastic and plastic properties [65,66], we obtain:

$$\boldsymbol{\sigma} = \mathbf{C}^{t} \Delta \boldsymbol{\varepsilon}_{el} + \boldsymbol{\sigma}^{t,rot}, \tag{46}$$

where $\mathbf{C}^{t}$ is the self-consistent estimate of elastic stiffness and $\boldsymbol{\sigma}^{t,rot}$ is stress from the beginning of the time increment rotated to the current configuration given by:

$$\boldsymbol{\sigma}^{t,rot} = \left\langle \Delta \mathbf{R}^{*t,(r)} \boldsymbol{\sigma}^{t,(r)} \Delta \mathbf{R}^{*t,(r)^{T}} \right\rangle. \tag{47}$$

The incremental rotation, $\Delta \mathbf{R}^{*t,(r)}$, is calculated as $\Delta \mathbf{R}^{*t,(r)} = \left(\mathbf{I} - \beta \mathbf{W}^{*t,(r)} \Delta t \right)^{-1} \left(\mathbf{I} + (1-\beta) \mathbf{W}^{*t,(r)} \Delta t \right)$, with $\beta = 0.5$ [96]. The elastic increment is given by:

$$\Delta \boldsymbol{\varepsilon}_{el} = \Delta \boldsymbol{\varepsilon} - \dot{\boldsymbol{\varepsilon}}_{vp} \Delta t, \tag{48}$$

where $\Delta \boldsymbol{\varepsilon}$ is the total strain increment and Δt is the time increment. Eq. (46) is decomposed into deviatoric and hydrostatic parts, which can be expressed in the vector form as:

$$\mathbf{s} - \mathbf{s}^{t,rot} - \mathbf{C}'^{t}_{5\times6} \left(\Delta \mathbf{e} - \mathbf{P}_{6\times5} \dot{\mathbf{e}}_{vp} \Delta t \right) = \mathbf{0}, \tag{49}$$

$$\sigma_m - \sigma_m^{t} - \frac{1}{3} \mathrm{tr} \left[\mathbf{C}^{t}_{6\times6} \left(\Delta \mathbf{e} - \mathbf{P}_{6\times5} \dot{\mathbf{e}}_{vp} \Delta t \right) \right] = 0 \tag{50}$$

where $\mathbf{s}$, $\mathbf{s}^{t,rot}$, $\dot{\mathbf{e}}_{vp}$, and $\Delta \mathbf{e}$ are the vector representation of tensors $\boldsymbol{\sigma}'$, $\boldsymbol{\sigma}'^{t,rot}$, $\dot{\boldsymbol{\varepsilon}}_{vp}$ and $\Delta \boldsymbol{\varepsilon}$ as:

$$\mathbf{s} = \begin{Bmatrix} \sigma'_{11} \\ \sigma'_{22} \\ \sigma'_{12} \\ \sigma'_{13} \\ \sigma'_{23} \end{Bmatrix}, \mathbf{s}^{t,rot} = \begin{Bmatrix} \sigma'^{t,rot}_{11} \\ \sigma'^{t,rot}_{22} \\ \sigma'^{t,rot}_{12} \\ \sigma'^{t,rot}_{13} \\ \sigma'^{t,rot}_{23} \end{Bmatrix}, \dot{\mathbf{e}}_{vp} = \begin{Bmatrix} \dot{\varepsilon}_{vp,11} \\ \dot{\varepsilon}_{vp,22} \\ \dot{\varepsilon}_{vp,12} \\ \dot{\varepsilon}_{vp,13} \\ \dot{\varepsilon}_{vp,23} \end{Bmatrix}, \Delta \mathbf{e} = \begin{Bmatrix} \Delta\varepsilon_{11} \\ \Delta\varepsilon_{22} \\ \Delta\varepsilon_{33} \\ 2\Delta\varepsilon_{12} \\ 2\Delta\varepsilon_{13} \\ 2\Delta\varepsilon_{23} \end{Bmatrix}. \tag{51}$$

$\mathbf{P}_{6\times5}$ is a transformation matrix that transforms the five-dimensional vector $\dot{\mathbf{e}}_{vp}$ into a six-dimensional representation compatible with $\Delta \mathbf{e}$ [97,98]. The $\mathbf{C}'^{t}_{5\times6}$ matrix representation of elastic stiffness produces a five-dimensional deviatoric stress vector when multiplied with six-dimensional strain increment vector $\Delta \mathbf{e}$. It is a matrix representation of tensor $C'^{t}_{ijkl} = C^{t}_{ijkl} - \frac{1}{3} C^{t}_{mnkl} \delta_{mn} \delta_{ij}$ with the third row removed. σ_m and σ_m^{t} are the hydrostatic portions of the stress tensors $\boldsymbol{\sigma}$ and $\boldsymbol{\sigma}^{t,rot}$, and $\mathbf{C}^{t}_{6\times6}$ is the matrix representation of the elastic stiffness tensor consistent with the definition of strain increment $\Delta \mathbf{e}$.

For a given strain increment, $\Delta \mathbf{e}$, Eq. (49) can be solved for visco-plastic strain rate, $\dot{\mathbf{e}}_{vp}$, using Newton's method. The residual and its Jacobian are:

$$\mathbf{F} \left(\dot{\mathbf{e}}_{vp} \right) = \mathbf{s} \left(\dot{\mathbf{e}}_{vp} \right) - \mathbf{s}^{t,rot} - \mathbf{C}'^{t}_{5\times6} \left(\Delta \mathbf{e} - \mathbf{P}_{6\times5} \dot{\mathbf{e}}_{vp} \Delta t \right) = \mathbf{0}, \tag{52}$$

$$\frac{\partial \mathbf{F}}{\partial \dot{\mathbf{e}}_{vp}} = \frac{\partial \mathbf{s}}{\partial \dot{\mathbf{e}}_{vp}} + \mathbf{C}'^{t}_{5\times6} \mathbf{P}_{6\times5} \Delta t, \tag{53}$$

Table 2
Solution procedure for the interaction equation — inner iterative loop for solving for slip resistance in grains.

(1)	Solve the interaction equation for stress, ${}^{j+1}\boldsymbol{\sigma}'^{(r),i+1}$, using Newton's method: $\dot{\boldsymbol{\varepsilon}}_{vp} - \dot{\gamma}_0 \sum_s \left(\frac{\mathbf{m}_{tot}^{s,t,(r)} \cdot {}^{j+1}\boldsymbol{\sigma}'^{(r),i+1}}{{}^{j}\tau_c^{\alpha,(r),i+1}} \right)^n \mathbf{m}^{s,t,(r)} = -\widetilde{\mathbf{M}}^i \left(\boldsymbol{\sigma}'^i - {}^{j+1}\boldsymbol{\sigma}'^{(r),i+1} \right)$
(2)	Calculate new guess for slip resistance ${}^{j+1}\tau_c^{\alpha,(r),i+1} = g\left(\left| \dot{\gamma}^s \left({}^{j+1}\boldsymbol{\sigma}'^{(r),i+1}, {}^{j}\tau_c^{\alpha,(r),i+1} \right) \right| \right).$
(3)	Test for convergence: **if** $\left(\sqrt{\frac{\sum_\alpha \left[{}^{j+1}\tau_c^{\alpha,(r),i+1} - {}^{j}\tau_c^{\alpha,(r),i+1} \right]^2}{\sum_\alpha \left[\frac{1}{2}\,{}^{j+1}\tau_c^{\alpha,(r),i+1} + \frac{1}{2}\,{}^{j}\tau_c^{\alpha,(r),i+1} \right]^2}} < \mathrm{tol} \right)$ **: exit** **else: go to** (1)

where the derivative $\frac{\partial \mathbf{s}}{\partial \dot{\mathbf{e}}_{vp}}$ can be approximated as $\frac{\partial \mathbf{s}}{\partial \dot{\mathbf{e}}_{vp}} \approx \mathbf{M}^{-1}$ [65,83]. The Newton iterations are facilitated using:

$$\dot{\mathbf{e}}_{vp}^{i+1} = \dot{\mathbf{e}}_{vp}^{i} - \left(\left. \frac{\partial \mathbf{F}}{\partial \dot{\mathbf{e}}_{vp}} \right|_{\dot{\mathbf{e}}_{vp}^{i}} \right)^{-1} \mathbf{F}\left(\dot{\mathbf{e}}_{vp}^{i} \right). \tag{54}$$

The iterative procedure over $\dot{\mathbf{e}}_{vp}^{i}$ terminates when the norm of the residual becomes smaller than the tolerance conveniently defined with respect to the current von Mises stress: $\left| \mathbf{F}\left(\dot{\mathbf{e}}_{vp}^{i} \right) \right| < 0.001\sigma_{vM}$. The deviatoric stress, $\mathbf{s}$, is available once the visco-plastic strain rate has converged and the hydrostatic portion, σ_m, can be calculated from Eq. (50).

In addition to the total stress at the end of the time increment, $\boldsymbol{\sigma}$, the FE solver also requires the Jacobian matrix obtained by differentiating the constitutive equation, i.e. Eq. (46):

$$\left(\frac{\partial \boldsymbol{\sigma}}{\partial \Delta \boldsymbol{\varepsilon}} \right)_{6\times 6} = \left[\mathbf{I}_{6\times 6} + \mathbf{C}_{6\times 6}^{t} \mathbf{P}_{6\times 5} \mathbf{M} \left(\frac{\partial \mathbf{s}}{\partial \boldsymbol{\sigma}} \right)_{5\times 6} \Delta t \right]^{-1} \mathbf{C}_{6\times 6}^{t}, \tag{55}$$

where $\left(\frac{\partial \mathbf{s}}{\partial \boldsymbol{\sigma}} \right)_{5\times 6}$ is the derivative of five-dimensional deviatoric stress with respect to the six independent components of stress tensor ordered analogously to the strain increment [82].

After the convergence of Newton's method, the texture is updated for plastic spin and inclusion spin. In addition, the shape of the ellipsoid is updated for the applied plastic deformation. Note that the texture and ellipsoid are already rotated for the macroscopic spin provided by the FE solver at the beginning of the time increment to ensure that they are in the same configuration as the strain increment and other quantities.

As was noted before, in a large number of implicit finite element implementations of crystal plasticity codes the state variables are held constant while the stress is updated implicitly [65,67,82,83]. The state variables are subsequently updated explicitly. Consequently, the magnitude of the current strain increment does not affect the current slip resistances and thus does not influence the current deviatoric stress magnitude, $\frac{\partial |\boldsymbol{\sigma}'|}{\partial |\Delta \boldsymbol{\varepsilon}|} = \sum_r \sum_s \frac{\partial |\boldsymbol{\sigma}'|}{\partial \tau_c^{s,(r),expl}} \frac{\partial \tau_c^{s,(r),expl}}{\partial |\Delta \boldsymbol{\varepsilon}|} = 0$. Therefore, the stress magnitude cannot increase regardless of the magnitude or direction of currently applied strain increment since it is bound to a constant yield surface defined by the slip resistances from the beginning of the time increment. There can be no loading and the stress can only move along the constant yield surface (neutral loading) or to the interior of the yield surface (unloading) [99]. On the other hand, the implicit evolution of slip resistances employed here causes the expansion of the yield surface with the increase of the currently applied strain increment and thus an increase in the stress magnitude. It should also be noted that an explicit evolution of the slip resistances before the evaluation of stress would achieve similar results as the implicit integration.

2.6. *Conversion of plastic work to heat*

During plastic deformation there is conversion of plastic work to heat known as adiabatic heating, which causes an increase in the sample temperature. At low strain rates (below 10^{-3} s^{-1}) the generation of heat is small since any heat is quickly conducted away from the specimen. Therefore, behavior is approximately isothermal. At higher strain rates (above 10 s^{-1}) there is no sufficient time for the generated heat to be conducted away. Therefore almost all plastic work is transferred into heat, and the conditions are adiabatic. For the strain rates between these two limiting values, the conditions are in-between adiabatic and isothermal. In what follows we define the expressions for the calculation of temperature increase due to adiabatic heating during high strain rate compression and impact simulations.

The governing equation for calculating the temperature at the end of the time increment, T, during compression test is given by the explicit Euler forward update [100]:

$$T = T^t + \eta\left(\dot{\varepsilon}\right)\xi \frac{\dot{W}^p}{\rho C_p}\Delta t, \tag{56}$$

where ξ is the fraction of plastic work converted into heat, ρ is density of Ta (taken for pure Ta as 16 640 kg/m^3 [30]), and C_p is the specific heat given as a function of temperature for Ta [72]:

$$C_p = A_0 + A_1 T^t + \frac{A_2}{\left(T^t\right)^2}, \tag{57}$$

with $A_0 = 145.5\ \frac{\mathrm{J}}{\mathrm{kgK}}$, $A_1 = 0.009544\ \frac{\mathrm{J}}{\mathrm{kgK}^2}$, and $A_2 = -68900\ \frac{\mathrm{J}}{\mathrm{kg}}\mathrm{K}$. $\dot{W}^p$ is the plastic work rate calculated as:

$$\dot{W}^p = \boldsymbol{\sigma}' \cdot \dot{\boldsymbol{\varepsilon}}_{vp}. \tag{58}$$

η is the adiabatic correction factor and represents a fraction of the heat retained within the compression specimen for the rates between $10^{-3}\ \mathrm{s}^{-1}$ and $10\ \mathrm{s}^{-1}$ when the compression test conditions are neither isothermal nor adiabatic [100]. It is calculated as:

$$\eta = \begin{cases} 0,\ \text{if}\ \dot{\varepsilon} < 10^{-3}\ \mathrm{s}^{-1} \\ 0.25\left(\log\dot{\varepsilon} + 3\right),\ \text{if}\ 10\ \mathrm{s}^{-1} > \dot{\varepsilon} > 10^{-3}\ \mathrm{s}^{-1} \\ 1,\ \text{if}\ \dot{\varepsilon} > 10\ \mathrm{s}^{-1}. \end{cases} \tag{59}$$

The fraction of plastic work converted into heat, ξ, is usually taken between 0.8 and 0.95. However, ξ varies with the material [101], and for Ta this value was measured to be close to 1.0 [102,103], which is what we used in all the simulations.

In the impact tests, the strain rates are well above 10 s^{-1}, requiring the consideration of the adiabatic conditions (Eq. (56)). In the case of forming processes where strain rates are such that the process cannot be considered neither adiabatic nor isothermal, it is recommended that the heat conduction be considered in coupled temperature–displacement FE analysis.

3. Remeshing and interpolation procedures for state variables including texture

During the FE simulations to large strains, the elements can become severely distorted, requiring remeshing. When the ratio of the longest edge to the shortest edge of the most distorted element reaches a value 7, the remeshing is triggered. The deformed part is imported as geometry into ABAQUS/CAE and completely remeshed using the ABAQUS Mesh module. After remeshing all variables defining the current state of the part require mapping/interpolation. Most of the state variables can be interpolated linearly except for the variables defining grain orientations. The latter will be interpolated using the spherical linear interpolation (Slerp) in the space of quaternions. Additionally, the deformation gradients, because they consist of both rotation and deformation, will be interpolated using a combination of the Slerp method and the linear shape functions method. In what follows, we describe the adopted interpolation procedures for field variables, grain orientations, and deformation gradients.

Fields of strain, stress, temperature, velocity, slip resistance within each grain, and dislocation densities within each grain are interpolated linearly using the finite element shape functions [104]. Shape functions of linear 3D elements can be viewed as a linear interpolation technique that can be easily applied to quantities available at both nodes and integration points. Fig. 2 illustrates the interpolation procedure in the Taylor impact simulation for the velocity component v_z, which is parallel to the cylinder axis. For a given integration point or node of the new mesh, the algorithm is:

(1) Determine the element of the old mesh to which the point belongs and calculate natural coordinates, (g, h, r), of the point within the element.

(2) Interpolate the variable value at the point of new mesh using nodal variables of the old mesh, x^i, and shape functions, $N^i\left(g, h, r\right)$,:

$$x = \mathbf{N} \cdot \mathbf{x}. \tag{60}$$

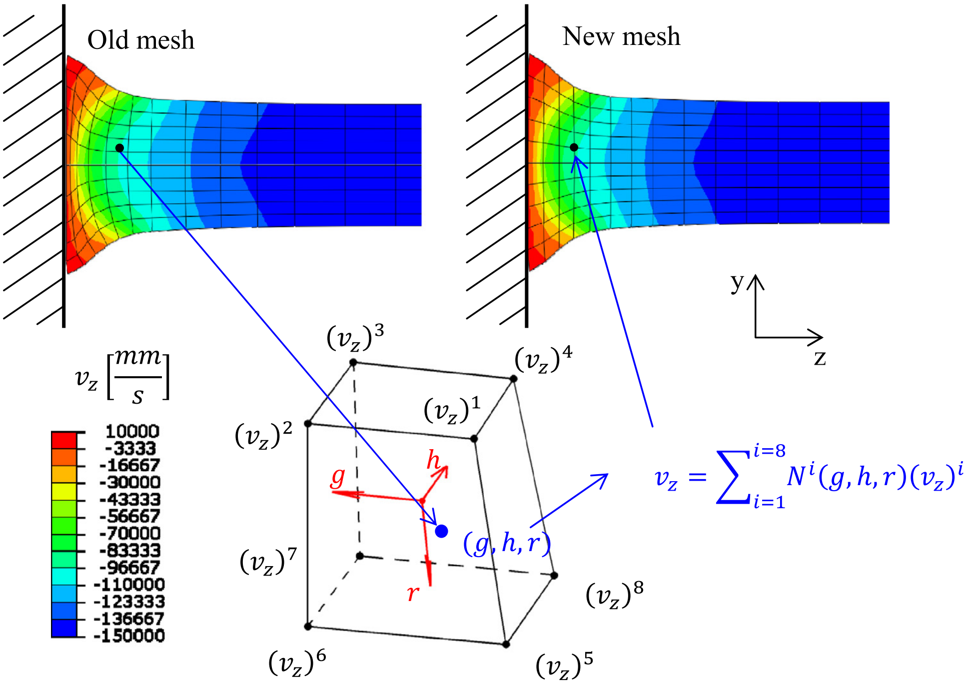

Fig. 2. Schematic showing the interpolation procedure, based on the finite element shape functions, for the calculation of the velocity component v_z at a point of new mesh using the velocity components $(v_z)^i$ at the element vertices from the old mesh. The contour plots verify accuracy of the interpolated field over the new mesh against the original field from the old mesh.

Fig. 2 also shows the old (deformed) and new mesh upon remeshing, along with the contours of velocity fields. The similarity between the fields in two meshes demonstrates the accuracy of the interpolation procedure for field variables. Due to interpolation and remeshing the stress equilibrium will be violated at the macro (FEA) and meso (VPSC) level. However, considering the similarity between meshes before and after remeshing the interpolated state is very close to the equilibrium. The equilibrium is enforced in the first increment after remeshing. The difference between equilibrated stress fields before and after remeshing is negligible. Some small discrepancy in the equivalent plastic strain rate fields before and after remeshing is observed for several nodes close to the center of the foot, which can be expected considering a very high gradient of the equivalent plastic strain rate in that region.

The crystal orientations of grains are interpolated using the spherical linear interpolation (Slerp) algorithm in the quaternion space [105,106]. Expression for spherical linear interpolation between two quaternions, $\mathbf{q}_1$ and $\mathbf{q}_2$, with parameter u going from 0 to 1 is given by:

$$\mathrm{Slerp}\,(\mathbf{q}_1, \mathbf{q}_2; u) = \frac{\sin\,(1-u)\,\theta}{\sin\theta}\mathbf{q}_1 + \frac{\sin u\theta}{\sin\theta}\mathbf{q}_2 \tag{61}$$

where $\mathbf{q}_1 \cdot \mathbf{q}_2 = \cos\theta$. Since the orientation of each grain within the polycrystal is interpolated separately, texture of the polycrystal is also indirectly interpolated. Fig. 3 shows three textures obtained by interpolating orientation of each grain between its initial orientation and final orientation after compression to a high strain, for three different values of the parameter u. The Slerp method imposes two constraints: (1) textures must be represented by the same number of discrete orientations and (2) pairing between the orientations from the discrete sets must be assumed. Due to these limitations the Slerp method is limited when compared to other probability distribution interpolation techniques [107–112]. However, it is quite convenient for the interpolation between textures of two polycrystals with the same initial texture after similar strain history. Other texture interpolation techniques are not investigated here since they would likely yield similar results considering that the texture does not vary appreciably within one element. In addition, there is an additional complication associated with the texture interpolation methods that are not based on the direct pairing of discrete orientations. Once the texture is interpolated and represented by the discrete set of

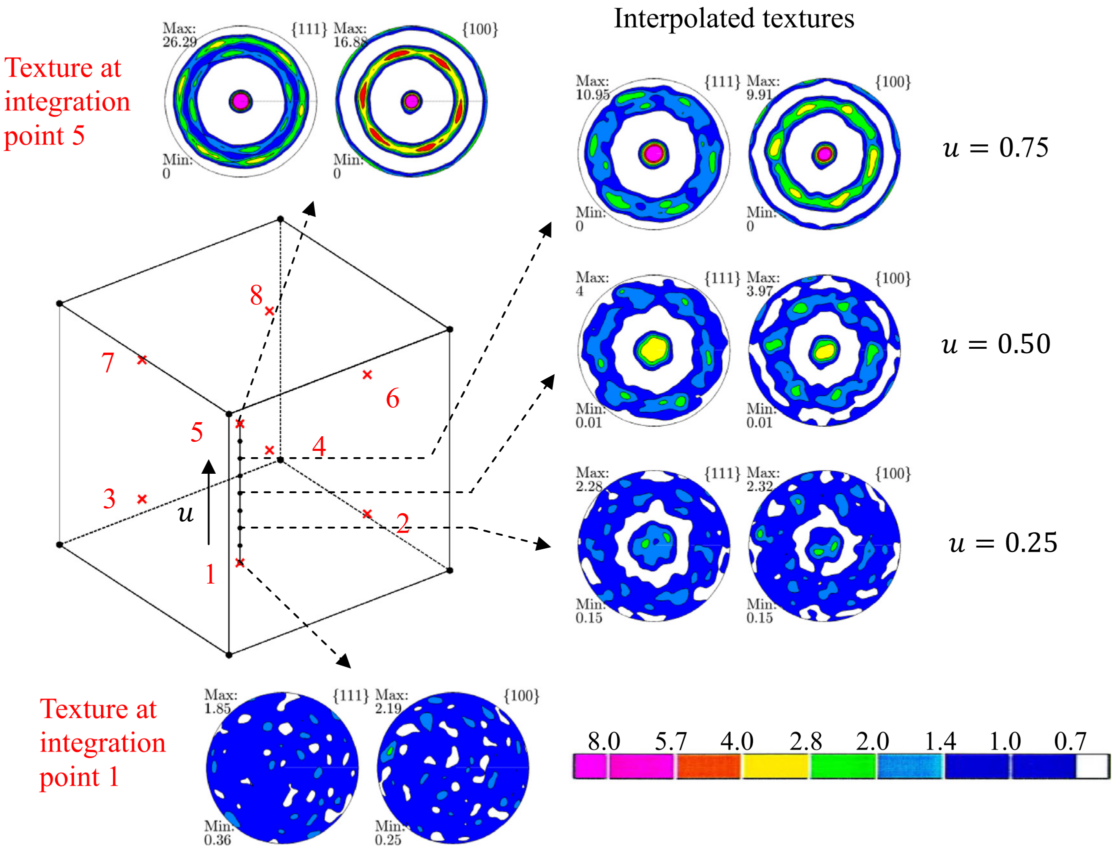

Fig. 3. Texture interpolation between two integration points using the Slerp algorithm. Three interpolated textures weighted between the two textures used in the interpolation are shown.

orientations, the interpolation of grain properties becomes an issue since there is no longer a natural pairing between the grains, which is preserved with the Slerp method.

The average grain shape is defined by the deformation gradient tensor. The interpolation of deformation gradient follows the algorithm given in [105]. The deformation gradient, **F**, is decomposed into a stretching tensor, **U**, and a rotation tensor, **R**, using the polar decomposition:

$$\mathbf{F} = \mathbf{RU}. \tag{62}$$

Each component of the stretch tensor, **U**, is independently interpolated using shape functions as described above. The rotation tensor, **R**, represents pure rotation and is thus transferred to quaternion form and interpolated using the Slerp algorithm.

4. Material and model calibration for strain rate and temperature sensitive deformation

The hardening parameters for commercially pure Ta were calibrated on a set of stress–strain curves reported in [30,72,113]. The Ta plate was prepared by melting ingots with the following composition (in weight ppm): C 12, O $<$ 50, N $<$ 10, H $<$ 5, W 60, Nb 250, and Ta balance [113]. The quasi-static and dynamic compression tests were performed at various temperatures on the cylindrical samples machined from the Ta plate. The cylindrical specimens had their axes in the through-thickness (TT) direction. Orientation distribution function (ODF) of the plate was derived from the experimental X-ray pole figures. {111} and {100}, pole figures of the derived ODF, are plotted in Fig. 4. The ODF was then approximated with 200 weighted orientations for simulations (Fig. 4b).

In the simulations, we assume grains are initially spherical and deform by $\left\{1\bar{1}0\right\}\langle 111\rangle$ and $\left\{11\bar{2}\right\}\langle 111\rangle$ slip modes. The initial slip resistance and hardening parameters of both modes are assumed to be the same. Constants for initial

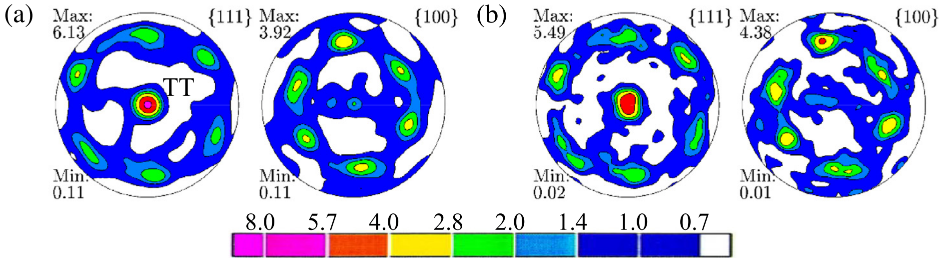

Fig. 4. {111} and {100} equal area projection-type pole figures showing initial texture of the tantalum plate: (a) measured data and (b) representation of the measured data using 200 weighted orientations for simulations. TT direction of the plate is in the center of the pole figures.

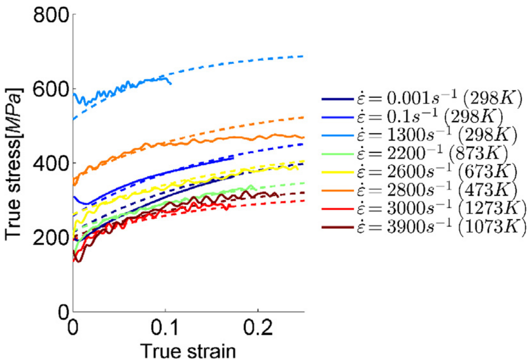

Fig. 5. Comparison between experimental (full line) and predicted (dashed line) compressive true stress–true strain curves for tantalum in the TT direction at various strain rates and temperatures.

slip resistance are determined first from the initial yield stresses at different temperatures and strain rates (Table 3). Next, the hardening parameters are calibrated and presented in Table 3. The predictions of the model are compared to the experimental stress–strain curves in Fig. 5, and good agreement is achieved.

5. Verification of VPSC with implicit hardening and application of FE-VPSC to impact

We begin by presenting the results, verifying the implicit hardening model within VPSC, and then present the predictions of the Taylor impact simulation by FE-VPSC.

5.1. Verification of the implicit hardening implementation within VPSC

Predictions of the VPSC model with implicit and explicit hardening are compared for the case of room temperature, quasi-static deformation to a true strain of 0.4. The strain increment was set to 0.001. Fig. 6a compares the stress–strain curves, while Fig. 6b compares the deformed textures. Good agreement is achieved, which is expected for any sufficiently low strain increment. Fig. 7 shows the influence of the strain increment on the results of the implicit hardening VPSC model. The decay in non-Schmid effects with strain is removed so that the differences in hardening behavior can be better observed. Negligible dependence of the stress–strain response on the magnitude of strain increment is observed. This is caused predominantly by the implicit updating of the dislocation densities (Eqs. (25) and (26)).

5.2. Taylor impact simulations

We use the FE-VPSC model calibrated for Ta to simulate the Taylor impact test of Ta cylinder reported in [20,30]. Taylor impact specimens were made from the Ta plate with the cylinder axis parallel to one of the in-plane directions. The length of the cylinder was 38.1 mm and the diameter was 7.62 mm, while the impact velocity was 175 m/s.

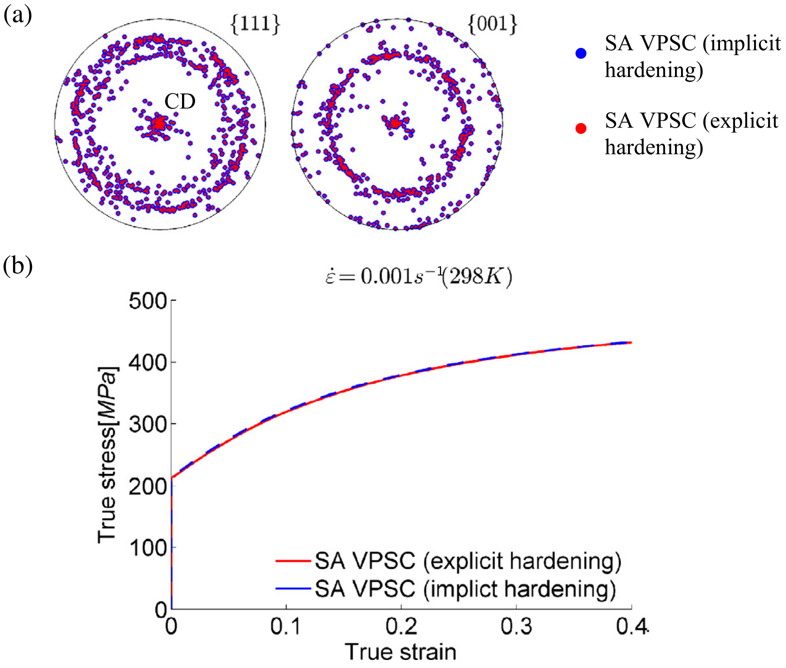

Fig. 6. Comparison of (a) texture evolution and (b) true stress–true strain response, calculated using explicit and implicit implementation of the dislocation density-based hardening law within VPSC for simple compression at room temperature under a strain rate of $\dot{\varepsilon} = 0.001$ s^{-1}.

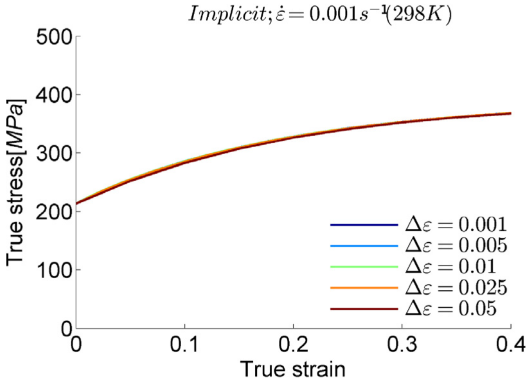

Fig. 7. Effect of the strain increment size used in predicting compressive true stress–true strain response of tantalum at room temperature under a strain rate of $\dot{\varepsilon} = 0.001$ s^{-1} with implicit hardening implementation in VPSC.

Geometric profiles of the cylinder after testing were reported for three different tests. In addition, texture was measured using X-rays at several axial positions for one of the cylinders after testing.

Simulation setup is given in Fig. 8a. ABAQUS STANDARD dynamic FE code is used. Due to symmetry of the process, only $\frac{1}{4}$ of the cylinder is modeled and meshed with 384 full integration brick elements (C3D8 — continuum 3D eight nodal). The symmetry boundary conditions are applied to the faces, along which cuts are made. A mesh sensitivity study was performed to exclude any appreciable effect of the mesh and element size on the results. Further refinement of the mesh leaves the results unchanged and only increases the computational time involved. The anvil target is modeled as a discrete rigid surface, and the friction between the cylinder and anvil is neglected. Consistent with the experiment, the initial velocity of the cylinder was 175 m/s. The initial texture embedded at each integration point plotted in the global frame of the FE model is given in Fig. 8b.

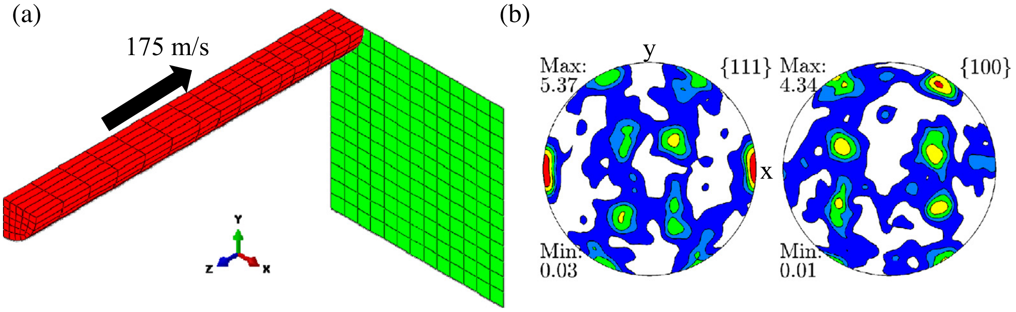

Fig. 8. (a) Finite element model of the Taylor impact test and (b) the initial texture of tantalum plotted in the global frame of the FE model (this texture is the same as the one in Fig. 3b but rotated to the global frame). The texture in (b) is embedded and evolved during deformation at each finite element integration point.

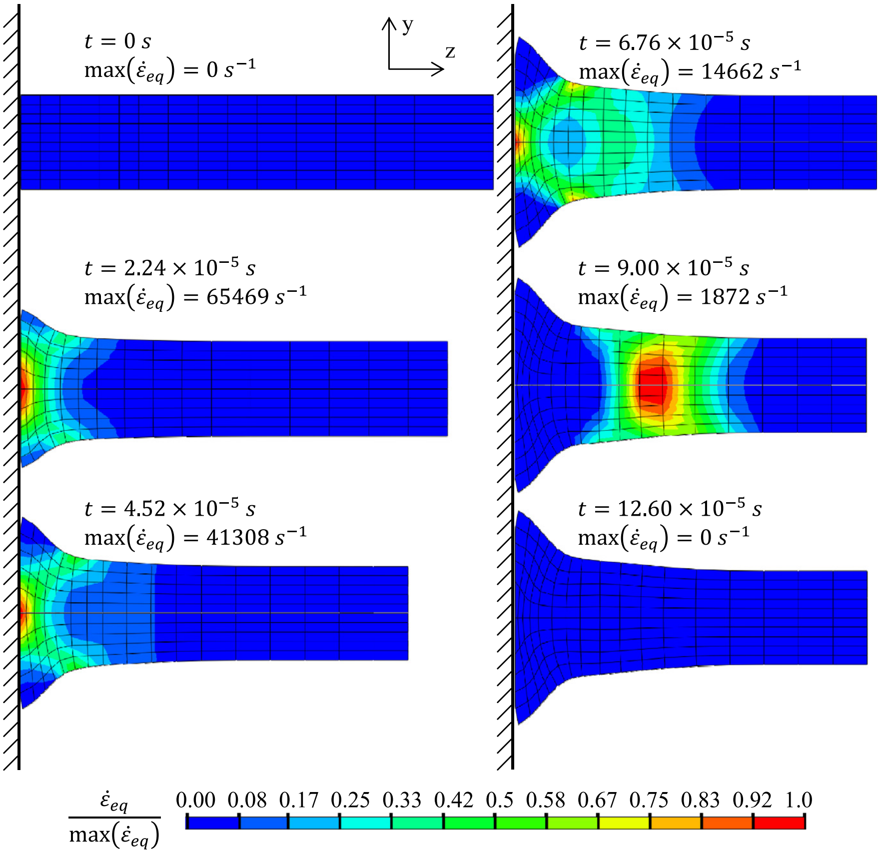

Fig. 9. Evolution of equivalent plastic strain rate field during the impact simulation at instants of time *t*. The strain rates used for the normalization are indicated in the figure for each contour plot.

The equivalent plastic strain rate, $\dot{\varepsilon}_{eq}$, fields developing in the cylinder during the simulation are shown in Fig. 9. Since the strain rate changes dramatically over the course of the simulation, it is not possible to facilitate the comparison between the distributions of equivalent plastic strain rate in the plots using the same scale. Hence, the fields were normalized with the maximal value of $\dot{\varepsilon}_{eq}$ present in the cylinder at that time. At the beginning of the impact, the highest $\dot{\varepsilon}_{eq}$ develops at the center of the foot and reaches values above 90 000 s^{-1}. As the deformation progresses, the $\dot{\varepsilon}_{eq}$ at the center of the foot decreases, and regions that are away from the foot and cylinder axis start deforming. Finally, at the end of the simulation, the plastic wave propagates toward the tail of the cylinder.

Table 3
Calibrated parameters of the dislocation density-based hardening model for tantalum.

	$\alpha = 1, \{1\bar{1}0\}\langle 111\rangle$ and $\alpha = 2, \{11\bar{2}\}\langle 111\rangle$
k_1^{α} [m]	3.75×10^7
g^{α}	0.005
D^{α} [MPa]	1200
q^{α}	5
A^{α} [MPa]	233.93
B^{α} [K]	209.03
C^{α}	0.14
G^{α} [MPa]	71.25

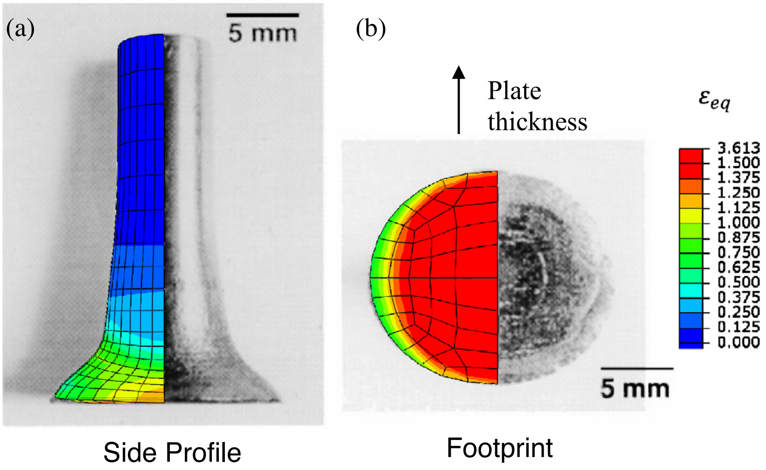

Fig. 10. Comparison of measured and predicted cylinder geometry after the test with the superimposed contours of equivalent plastic strain over the latter.

Fig. 10 compares the side profile and footprint of the simulated cylinder after the impact with photographs of the cylinder geometry after the test. The plastic deformation is highly heterogeneous, with the highest equivalent plastic strains occurring at the center of the foot and reaching values above 3.6. On the other hand, the tail of the cylinder is not experiencing any plastic deformation. In addition, the shape of the footprint is ellipsoidal, indicating that the deformation in lateral directions is also non-uniform.

The deformed major and minor profiles are compared with the experimental measurements in Fig. 11a. Radial strains are calculated based on the profiles as $\varepsilon_r = \ln \frac{d}{d_0}$ and plotted as a function of axial position in Fig. 11b. The difference between major and minor profiles is quantified with the R-value, calculated as $\varepsilon_r^{major}/\varepsilon_r^{minor}$. The results are plotted in Fig. 11c as a function of axial position. The observed difference between major and minor profiles is driven by the initial texture and subsequent texture evolution. The TT is the hard direction, which is along the minor profile of the cylinder. Due to the texture evolution, the anisotropy of the material changes, and at higher strains, the TT direction actually becomes the softest.

Fig. 12 compares the predicted and measured footprints. The initial footprint is plotted with dashed line as a reference to easily assess the amount of plastic deformation at the foot.

The large heterogeneity of plastic distortions in the axial direction induces a variation of microstructural evolution. The texture variation along the axis of the cylinder is compared with the experimental measurements at four axial locations: 9.2 mm, 6.5 mm, 1.6 mm, and 0.5 mm from the impact surface in Fig. 13. At location furthest away from the foot, the texture resembles the initial one since plastic deformation is negligible. As we move toward the foot we see development of BCC compression texture with {111} and {001} parallel to the compression direction [114,115]. Agreement of the main texture features between simulation and experiment is good. However, it is noted that simulated textures close to the foot display very high intensities. This is likely caused by the fact that in the VPSC model,

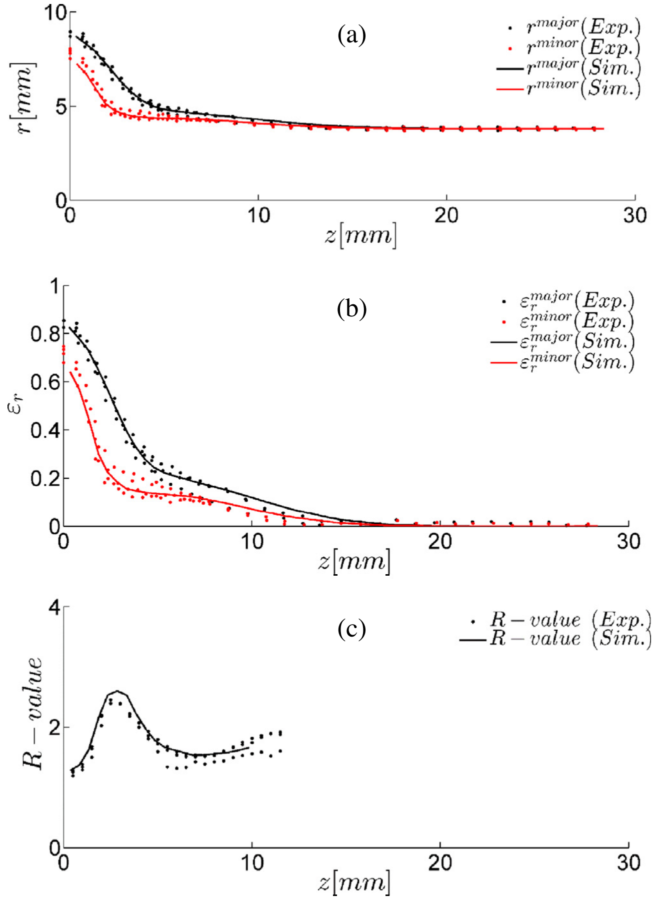

Fig. 11. Predicted by FE-VPSC (solid line) and experimentally measured (dots) post-test geometrical characteristics of the cylinder – (a) radius, (b) radial strains, and (c) R-values – plotted as functions of axial distance from the foot, z.

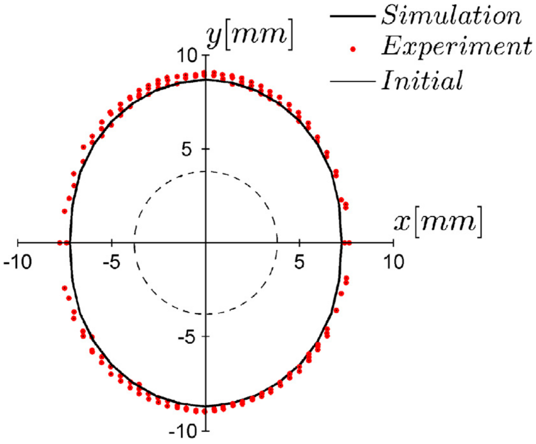

Fig. 12. Comparison of predicted and measured footprint geometry. As a reference, the initial cross-section geometry is plotted using the dashed line.

each grain is represented with only one orientation: uniform within the grain domain, which causes the predicted textures to be consistently stronger than the measured ones [9,116]. Accounting for intragranular misorientation

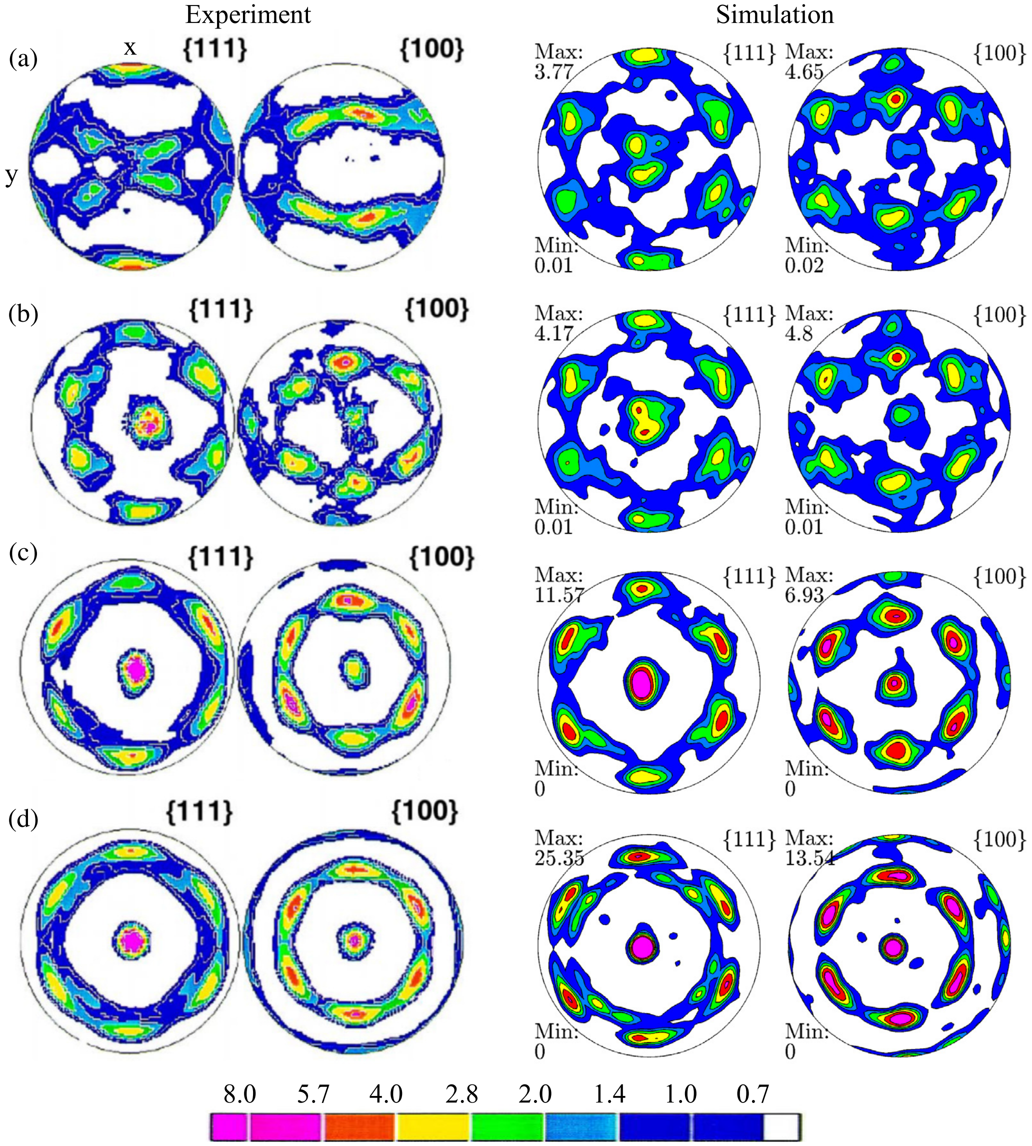

Fig. 13. Comparison of measured (by X-ray diffraction) and predicted texture evolution in the cylinder after the impact at (a) 9.2 mm, (b) 6.5 mm, (c) 1.6 mm, and (d) 0.5 mm away from the foot.

distributions using a second order moments within VPSC is aimed at relaxing typically predicted texture intensities by VPSC [117,118].

Very high strain rates and adiabatic heating are two competing mechanisms that influence flow stress, especially at the foot of the cylinder. The very high strain rate causes an increase in the resistance to intrinsic barriers, giving rise to a higher flow stress, while the increase in temperature lowers it. It is found that the temperature effects are stronger than the strain rate effects and the deformation, particularly at the center of the foot, is extremely high. Temperature at this region reaches almost 1000 °C which is still considerably below the melting temperature of Ta (3017 °C). Complex dependence of the flow stress on temperature and strain rate is accounted for using the thermally activated glide. The anisotropic plastic flow of Ta during the impact is primarily governed by the evolution of crystallographic texture, while the non-Schmid effects do not contribute appreciably mainly due to large plastic strain levels. Since the model developed here is texture-sensitive, evolves texture, and captures the rate and temperature dependence of flow stress, it is able to successfully capture the geometrical changes of the cylinder in a numerically stable manner. Future work will concentrate on incorporating damage criteria to facilitate coupled plasticity-damage simulations under high strain rate deformation.

6. Conclusions

This work presented an implementation of VPSC with removed rate sensitivity coming from the single crystal power-law flow rule into implicit finite elements (FE-VPSC) to enable the prediction of high strain rate and impact deformation of polycrystals. The implementation permits the description of the complex strain rate sensitivity of a material solely through the thermally activated dislocation density-based hardening law. As a result, magnitudes of flow stress can be accurately calculated during high strain rate deformation. The implementation required the development of an implicit numerical scheme for the hardening law within VPSC to enable the prediction of high strain rate and impact deformation. Moreover, deformation of individual single crystals in the model is activated not only from the resolved shear stress along the direction of slip (Schmid law), but also from shear stresses resolved along directions orthogonal to the slip direction and the three normal stress components (non-Schmid effects). Therefore, the model is capable of predicting the coupled texture and non-Schmid effects on anisotropic flow of BCC polycrystals. The developed model was used for the prediction of deformation behavior of Ta during high strain rate conditions, including the Taylor impact of a cylindrical specimen. Since the impact simulations required remeshing and interpolation of state variables, the spherical linear interpolation algorithm in the space of quaternions is implemented to facilitate the interpolation of texture. Adiabatic heating was also considered by the model. The predicted deformed shape of the cylinder is compared to the corresponding experimental measurements, and good agreement is achieved. Furthermore, the predicted texture evolution at several locations along the cylinder axis is also compared with measurements, and good agreement is achieved. It is found that the anisotropic plastic flow of Ta during impact is primarily governed by the evolution of crystallographic texture, while the non-Schmid effects do not contribute appreciably, mainly due to the large plastic strain levels and temperature increase. The developed FE-VPSC model can be broadly applied to understanding and predicting microstructure–property relationships in high strain rate deformation processes that generate spatially and temporarily heterogeneous mechanical fields.

Acknowledgments

This research was sponsored by the U.S. National Science Foundation and was accomplished under the CAREER grant no. CMMI-1650641. The authors would like to thank Dr. John F. Bingert for supplying the Taylor impact testing and characterization data sets.

Appendix

Below, we present the derivation of individual terms of Eq. (35). The superscript denoting grain number, r, is dropped for simplicity.

Term (1):

$$\frac{\partial \dot{\boldsymbol{\varepsilon}}_{vp}}{\partial \boldsymbol{\sigma}'} = \dot{\gamma}_0 \sum_{\alpha} \left\{ \sum_{s(\alpha)} n \left(\frac{\mathbf{m}_{tot}^{s,t} \cdot \boldsymbol{\sigma}'}{\tau_c^{\alpha}} \right)^{n-1} \mathbf{m}^{s,t} \otimes \mathbf{m}_{tot}^{s,t} \right\} \tag{A.1}$$

Term (2):

$$\frac{\partial \dot{\boldsymbol{\varepsilon}}_{vp}}{\partial \tau_c^{\alpha}} = -\sum_{s(\alpha)} n \underbrace{\dot{\gamma}_0 \left(\frac{\mathbf{m}_{tot}^{s,t} \cdot \boldsymbol{\sigma}}{\tau_c^{\alpha}} \right)^{n}}_{\dot{\gamma}^s} \frac{1}{\tau_c^{\alpha}} \mathbf{m}^{s,t} = -\sum_{s(\alpha)} n \dot{\gamma}^s \frac{1}{\tau_c^{\alpha}} \mathbf{m}^{s,t} \tag{A.2}$$

Term (3):

We assume there is a function τ_c^{α} that maps deviatoric stress directly to slip resistance at the end of the time increment given by the implicit equation:

$$\tau_c^{\alpha}\left(\boldsymbol{\sigma}'\right) = g\left(\left|\dot{\gamma}^s\left(\boldsymbol{\sigma}', \tau_c^{\alpha}\left(\boldsymbol{\sigma}'\right)\right)\right|\right). \tag{A.3}$$

Function g maps the absolute shear rates to slip resistance at the end of the time increment and is defined by the hardening law. In order to obtain derivatives of slip resistance w.r.t. deviatoric stress, we differentiate both sides of the equation:

$$\frac{\partial \tau_c^\alpha}{\partial \boldsymbol{\sigma}} = \frac{\partial g}{\partial \left|\dot{\gamma}^{s'}\right|} \frac{\partial \left|\dot{\gamma}^{s'}\right|}{\partial \boldsymbol{\sigma}'} + \frac{\partial g}{\partial \left|\dot{\gamma}^{s'}\right|} \frac{\partial \left|\dot{\gamma}^{s'}\right|}{\partial \tau_c^{\alpha'}} \frac{\partial \tau_c^\alpha}{\partial \boldsymbol{\sigma}'} \tag{A.4}$$

If we consider slip resistance and shear rates as vectors with length equal to number of slip modes and systems, respectively, we get:

$$\frac{\partial \boldsymbol{\tau}_c}{\partial \boldsymbol{\sigma}'} = \frac{\partial \mathbf{g}}{\partial \left|\dot{\boldsymbol{\gamma}}\right|} \frac{\partial \left|\dot{\boldsymbol{\gamma}}\right|}{\partial \boldsymbol{\sigma}'} + \frac{\partial \mathbf{g}}{\partial \left|\dot{\boldsymbol{\gamma}}\right|} \frac{\partial \left|\dot{\boldsymbol{\gamma}}\right|}{\partial \boldsymbol{\tau}_c} \frac{\partial \boldsymbol{\tau}_c}{\partial \boldsymbol{\sigma}'} \tag{A.5}$$

where | | denotes the absolute value. From here we can calculate the derivatives of slip resistance w.r.t. stress as:

$$\frac{\partial \boldsymbol{\tau}_c}{\partial \boldsymbol{\sigma}'} = \left[\mathbf{I}_{n_\alpha \times n_\alpha} - \frac{\partial \mathbf{g}}{\partial \left|\dot{\boldsymbol{\gamma}}\right|} \frac{\partial \left|\dot{\boldsymbol{\gamma}}\right|}{\partial \boldsymbol{\tau}_c}\right]^{-1} \frac{\partial \mathbf{g}}{\partial \left|\dot{\boldsymbol{\gamma}}\right|} \frac{\partial \left|\dot{\boldsymbol{\gamma}}\right|}{\partial \boldsymbol{\sigma}'} \tag{A.6}$$

where $\mathbf{I}_{n_\alpha \times n_\alpha}$ is an identity matrix with dimensions defined by the number of slip modes n_α. The derivatives appearing in the above equation are calculated as:

$$\frac{\partial \left|\dot{\gamma}^s\right|}{\partial \boldsymbol{\sigma}'} = \dot{\gamma}_0 n \left(\frac{\left|\mathbf{m}_{tot}^{s,t} \cdot \boldsymbol{\sigma}'\right|}{\tau_c^\alpha}\right)^{n-1} \frac{1}{\tau_c^\alpha} \mathbf{m}^{s,t} \tag{A.7}$$

$$\frac{\partial \left|\dot{\gamma}^s\right|}{\partial \tau_c^\alpha} = \begin{cases} -\dot{\gamma}_0 n \left(\dfrac{\left|\mathbf{m}_{tot}^{s,t} \cdot \boldsymbol{\sigma}'\right|}{\tau_c^\alpha}\right)^{n-1} \dfrac{\left|\mathbf{m}_{tot}^{s,t} \cdot \boldsymbol{\sigma}'\right|}{\tau_c^{\alpha 2}}; \text{ if } s \in \alpha \\ 0; \text{ if } s \notin \alpha \end{cases} \tag{A.8}$$

The term $\frac{\partial \mathbf{g}}{\partial |\dot{\boldsymbol{\gamma}}|}$ represents the derivative of slip resistance w.r.t. absolute shear rates, and it is defined separately for different hardening laws. We use dislocation-based hardening law, where only forest and debris terms depend on the shear rates through the dislocation densities (Eq. (20)). The derivatives of the slip resistance are:

$$\frac{\partial \tau_c^\alpha}{\partial \left|\dot{\gamma}^s\right|} = \frac{\partial \tau_{for}^\alpha}{\partial \rho_{for}^{\alpha'}} \frac{\partial \rho_{for}^{\alpha'}}{\partial \left|\dot{\gamma}^s\right|} + \frac{\partial \tau_{deb}^\alpha}{\partial \rho_{deb}} \frac{\partial \rho_{deb}}{\partial \left|\dot{\gamma}^s\right|} \tag{A.9}$$

where the individual terms are (no summation over repeated indices):

$$\frac{\partial \tau_{for}^\alpha}{\partial \rho_{for}^{\alpha'}} = b^\alpha \mu \frac{1}{2} \frac{1}{\sqrt{\sum_{\alpha'} \chi^{\alpha\alpha'} \rho_{for}^{\alpha'}}} \chi^{\alpha\alpha'} \tag{A.10}$$

$$\frac{\partial \rho_{for}^\alpha}{\partial \left|\dot{\gamma}^s\right|} = \left\{1 - \frac{1}{2}\left[\frac{1}{2} k_1 \frac{1}{\sqrt{\rho_{for}^\alpha}} - k_2\right] \sum_{s(\alpha)} \left|\dot{\gamma}^s\right| \Delta t\right\}^{-1} \frac{1}{2}\left[\frac{\partial \rho_{for}^\alpha}{\partial \gamma^\alpha}\left(\rho_{for}^{\alpha,t}\right) + \frac{\partial \rho_{for}^\alpha}{\partial \gamma^\alpha}\left(\rho_{for}^\alpha\right)\right]; \text{ with } s \in \alpha \tag{A.11}$$

$$\frac{\partial \tau_{deb}^\alpha}{\partial \rho_{deb}} = -k_{deb} \mu b^\alpha \left[\log\left(b^\alpha \sqrt{\rho_{deb}}\right) + 1\right] \frac{1}{2} \frac{1}{\sqrt{\rho_{deb}}} \tag{A.12}$$

$$\begin{aligned} \frac{\partial \rho_{deb}}{\partial \left|\dot{\gamma}^s\right|} = {} & \left[1 - \frac{1}{2} \frac{\Delta \rho_{deb}}{\rho_{deb}}\right]^{-1} \left\{\frac{1}{2} \sqrt{\rho_{deb}} q^{\alpha'} b^{\alpha'} k_2 \frac{\partial \rho_{for}^{\alpha'}}{\partial \left|\dot{\gamma}^s\right|} \sum_{s(\alpha)} \left|\dot{\gamma}^s\right| \Delta t + \sqrt{\rho_{deb}} q^{\alpha'} b^{\alpha'} 0.5 k_2 \right. \\ & \left. \left[\rho_{for}^{\alpha',t} + \rho_{for}^{\alpha'}\right] \Delta t \right\}; \text{ with } s \in \alpha' \end{aligned} \tag{A.13}$$

where

$$\Delta\rho_{deb} = \sqrt{\rho_{deb}} \sum_{\alpha} q^{\alpha} b^{\alpha} \frac{1}{2} \left[\frac{\partial \rho^{\alpha}_{rem,for}}{\partial \gamma^{\alpha}} \left(\rho^{\alpha,t}_{for} \right) + \frac{\partial \rho^{\alpha}_{rem,for}}{\partial \gamma^{\alpha}} \left(\rho^{\alpha}_{for} \right) \right] \sum_{s(\alpha)} \left| \dot{\gamma}^{s} \right| \Delta t. \tag{A.14}$$

References

[1] Fabricated Products High Performance Solutions, H.C. Starck Inc., 2013.
[2] L. Hesla, Seamless cavity performance, International Linear Collider Newsline, 2011.
[3] J. Shields Jr, P. Lipetzky, A. Mueller, Fracture Toughness of 6.4 mm arc-cast molybdenum and molybdenum-TZM plate at room temperature and 300 deg C, in: DE-AC11-98PN38206, 1999.
[4] R.W. Buckman, New applications for tantalum and tantalum alloys, JOM 52 (2000) 40–41.
[5] J. Christian, Some surprising features of the plastic deformation of body-centered cubic metals and alloys, Metall. Mater. Trans. A 14 (1983) 1237–1256.
[6] S. Chen, G. Gray, Constitutive behavior of tantalum and tantalum-tungsten alloys, Metall. Mater. Trans. A 27 (1996) 2994–3006.
[7] C.A. Bronkhorst, G.T. Gray III, F.L. Addessio, V. Livescu, N. Bourne, S. McDonald, P. Withers, Response and representation of ductile damage under varying shock loading conditions in tantalum, J. Appl. Phys. 119 (2016) 085103.
[8] K. Hoge, A. Mukherjee, The temperature and strain rate dependence of the flow stress of tantalum, J. Mater. Sci. 12 (1977) 1666–1672.
[9] U.F. Kocks, C.N. Tomé, H.-R. Wenk, Texture and Anisotropy, Cambridge University Press, Cambridge, UK, 1998.
[10] U.F. Kocks, H. Mecking, Physics and phenomenology of strain hardening: the FCC case, Prog. Mater. Sci. 48 (2003) 171–273.
[11] R.J. Asaro, A. Needleman, Texture development and strain hardening in rate dependent polycrystals, Acta Metall. Mater. 33 (1985) 923–953.
[12] H.F. Al-Harbi, M. Knezevic, S.R. Kalidindi, Spectral approaches for the fast computation of yield surfaces and first-order plastic property closures for polycrystalline materials with cubic-triclinic textures, CMC: Comput. Mater. Continua 15 (2010) 153–172.
[13] J.B. Shaffer, M. Knezevic, S.R. Kalidindi, Building texture evolution networks for deformation processing of polycrystalline fcc metals using spectral approaches: Applications to process design for targeted performance, Int. J. Plast. 26 (2010) 1183–1194.
[14] K.K. Mathur, P.R. Dawson, On modelling the development of crystallographic texture in bulk forming processes, Int. J. Plast. 5 (1989) 67–94.
[15] M. Zecevic, I.J. Beyerlein, M. Knezevic, Coupling elasto-plastic self-consistent crystal plasticity and implicit finite elements: Applications to compression, cyclic tension-compression, and bending to large strains, Int. J. Plast. 93 (2017) 187–211.
[16] M. Zecevic, M. Knezevic, Modeling of sheet metal forming based on implicit embedding of the elasto-plastic self-consistent formulation in shell elements: Application to cup drawing of AA6022-T4, JOM 69 (2017) 922–929.
[17] M. Knezevic, B. Drach, M. Ardeljan, I.J. Beyerlein, Three dimensional predictions of grain scale plasticity and grain boundaries using crystal plasticity finite element models, Comput. Methods Appl. Mech. Engrg. 277 (2014) 239–259.
[18] M. Ardeljan, R.J. McCabe, I.J. Beyerlein, M. Knezevic, Explicit incorporation of deformation twins into crystal plasticity finite element models, Comput. Methods Appl. Mech. Engrg. 295 (2015) 396–413.
[19] G.I. Taylor, The use of flat-ended projectiles for determining dynamic yield stress. I. Theoretical considerations, in: Proceedings of the Royal Society of London A: Mathematical, Physical and Engineering Sciences, The Royal Society, 1948, pp. 289–299.
[20] P. Maudlin, G. Gray, C. Cady, G. Kaschner, High–rate material modelling and validation using the Taylor cylinder impact test, Phil. Trans. R. Soc. A 357 (1999) 1707–1729.
[21] E. Lee, S. Tupper, Analysis of plastic deformation in a steel cylinder striking a rigid target, J. Appl. Mech. 21 (1954) 63–70.
[22] J. Hawkyard, A theory for the mushrooming of flat-ended projectiles impinging on a flat rigid anvil, using energy considerations, Int. J. Mech. Sci. 11 (1969) 313–333.
[23] G.R. Johnson, W.H. Cook, A constitutive model and data for metals subjected to large strains, high strain rates and high temperatures, in: Proceedings of the 7th International Symposium on Ballistics, The Hague, The Netherlands, 1983, pp. 541–547.
[24] F.J. Zerilli, R.W. Armstrong, Description of tantalum deformation behavior by dislocation mechanics based constitutive relations, J. Appl. Phys. 68 (1990) 1580–1591.
[25] F.J. Zerilli, R.W. Armstrong, Dislocation-mechanics-based constitutive relations for material dynamics calculations, J. Appl. Phys. 61 (1987) 1816–1825.
[26] D.J. Bammann, Modeling temperature and strain rate dependent large deformations of metals, Appl. Mech. Rev. 43 (1990) S312–S319.
[27] D. Steinberg, C. Lund, A constitutive model for strain rates from 10− 4 to 106 s−, J. Appl. Phys. 65 (1989) 1528–1533.
[28] D.L. Preston, D.L. Tonks, D.C. Wallace, Model of plastic deformation for extreme loading conditions, J. Appl. Phys. 93 (2003) 211–220.
[29] P. Follansbee, U. Kocks, A constitutive description of the deformation of copper based on the use of the mechanical threshold stress as an internal state variable, Acta Metall. 36 (1988) 81–93.
[30] P. Maudlin, J. Bingert, J. House, S. Chen, On the modeling of the Taylor cylinder impact test for orthotropic textured materials: experiments and simulations, Int. J. Plast. 15 (1999) 139–166.
[31] B. Revil-Baudard, O. Cazacu, P. Flater, G. Kleiser, Plastic deformation of high-purity α-titanium: Model development and validation using the Taylor cylinder impact test, Mech. Mater. 80, Part B (2015) 264–275.
[32] B. Plunkett, O. Cazacu, R.A. Lebensohn, F. Barlat, Elastic-viscoplastic anisotropic modeling of textured metals and validation using the Taylor cylinder impact test, Int. J. Plast. 23 (2007) 1001–1021.
[33] S. Kok, A.J. Beaudoin, D.A. Tortorelli, A polycrystal plasticity model based on the mechanical threshold, Int. J. Plast. 18 (2002) 715–741.
[34] M. Kothari, L. Anand, Elasto-viscoplastic constitutive equations for polycrystalline metals: application to tantalum, J. Mech. Phys. Solids 46 (1998) 51–83.

[35] W. Kocks, Thermodynamics and kinetics of slip, Prog. Mater. Sci. 19 (1975) 291.
[36] E. Schmid, W. Boas, Plasticity of Crystals with Special Reference to Metals, English translation F.A. Hughes, London, 1950.
[37] M.a.-S. Duesbery, V. Vitek, Plastic anisotropy in bcc transition metals, Acta Mater. 46 (1998) 1481–1492.
[38] B. Peeters, S.R. Kalidindi, C. Teodosiu, P.V. Houtte, E. Aernoudt, A theoretical investigation of the influence of dislocation sheets on evolution of yield surfaces in single-phase BCC polycrystals, J. Mech. Phys. Solids 50 (2002) 783–807.
[39] L. Stainier, A.M. Cuitiño, M. Ortiz, A micromechanical model of hardening, rate sensitivity and thermal softening in BCC single crystals, J. Mech. Phys. Solids 50 (2002) 1511–1545.
[40] G. Taylor, Thermally-activated deformation of BCC metals and alloys, Prog. Mater. Sci. 36 (1992) 29–61.
[41] Z.Q. Wang, I.J. Beyerlein, An atomistically-informed dislocation dynamics model for the plastic anisotropy and tension–compression asymmetry of BCC metals, Int. J. Plast. 27 (2011) 1471–1484.
[42] C. Alleman, S. Ghosh, D. Luscher, C.A. Bronkhorst, Evaluating the effects of loading parameters on single-crystal slip in tantalum using molecular mechanics, Phil. Mag. 94 (2014) 92–116.
[43] J. Chang, W. Cai, V.V. Bulatov, S. Yip, Dislocation motion in BCC metals by molecular dynamics, Mater. Sci. Eng. A 309 (2001) 160–163.
[44] P. Gordon, T. Neeraj, Y. Li, J. Li, Screw dislocation mobility in BCC metals: the role of the compact core on double-kink nucleation, Modelling Simulation Mater. Sci. Eng. 18 (2010) 085008.
[45] H. Lim, C.R. Weinberger, C.C. Battaile, T.E. Buchheit, Application of generalized non-Schmid yield law to low-temperature plasticity in bcc transition metals, Modelling Simulation Mater. Sci. Eng. 21 (2013) 045015.
[46] R. Gröger, V. Racherla, J.L. Bassani, V. Vitek, Multiscale modeling of plastic deformation of molybdenum and tungsten: II. Yield criterion for single crystals based on atomistic studies of glide of screw dislocations, Acta Mater. 56 (2008) 5412–5425.
[47] Q. Qin, J.L. Bassani, Non-Schmid yield behavior in single crystals, J. Mech. Phys. Solids 40 (1992) 813–833.
[48] V. Vitek, M. Mrovec, R. Gröger, J. Bassani, V. Racherla, L. Yin, Effects of non-glide stresses on the plastic flow of single and polycrystals of molybdenum, Mater. Sci. Eng. A 387 (2004) 138–142.
[49] M. Dao, R.J. Asaro, Non-Schmid effects and localized plastic flow in intermetallic alloys, Mater. Sci. Eng. A 170 (1993) 143–160.
[50] M. Knezevic, I.J. Beyerlein, M.L. Lovato, C.N. Tomé, A.W. Richards, R.J. McCabe, A strain-rate and temperature dependent constitutive model for BCC metals incorporating non-Schmid effects: Application to tantalum–tungsten alloys, Int. J. Plast. 62 (2014) 93–104.
[51] M. Knezevic, M. Zecevic, I.J. Beyerlein, A. Bhattacharyya, R.J. McCabe, Predicting texture evolution in ta and Ta-10W alloys using polycrystal plasticity, JOM 67 (2015) 2670–2674.
[52] H. Mecking, U.F. Kocks, Kinetics of flow and strain-hardening, Acta Metall. Mater. 29 (1981) 1865–1875.
[53] M. Knezevic, M. Zecevic, I.J. Beyerlein, R.A. Lebensohn, A numerical procedure enabling accurate descriptions of strain rate-sensitive flow of polycrystals within crystal visco-plasticity theory, Comput. Methods Appl. Mech. Engrg. 308 (2016) 468–482.
[54] G.I. Taylor, Plastic strain in metals, J. Inst. Met. 62 (1938) 307–324.
[55] J.W. Hutchinson, Bounds and self-consistent estimates for creep of polycrystalline materials, Proc. R. Soc. A 348 (1976) 101–126.
[56] I.J. Beyerlein, C.N. Tomé, A dislocation-based constitutive law for pure Zr including temperature effects, Int. J. Plast. 24 (2008) 867–895.
[57] R.A. Lebensohn, C.N. Tomé, A self-consistent anisotropic approach for the simulation of plastic deformation and texture development of polycrystals: Application to zirconium alloys, Acta Metall. Mater. 41 (1993) 2611–2624.
[58] M. Knezevic, J. Crapps, I.J. Beyerlein, D.R. Coughlin, K.D. Clarke, R.J. McCabe, Anisotropic modeling of structural components using embedded crystal plasticity constructive laws within finite elements, Int. J. Mech. Sci. 105 (2016) 227–238.
[59] M. Zecevic, M. Knezevic, I.J. Beyerlein, R.J. McCabe, Texture formation in orthorhombic alpha-uranium under simple compression and rolling to high strains, J. Nucl. Mater. 473 (2016) 143–156.
[60] B. Plunkett, O. Cazacu, R. Lebensohn, F. Barlat, Elastic-viscoplastic anisotropic modeling of textured metals and validation using the Taylor cylinder impact test, Int. J. Plast. 23 (2007) 1001–1021.
[61] P. Maudlin, S. Schiferl, Computational anisotropic plasticity for high-rate forming applications, Comput. Methods Appl. Mech. Engrg. 131 (1996) 1–30.
[62] E. Orowan, Problems of plastic gliding, Proc. Phys. Soc. 52 (1940) 8.
[63] A.S. Krausz, H. Eyring, Deformation Kinetics, Wiley, 1975.
[64] L.R.A.C.N. Tomé, Manual for Code Viscoplastic Self-consistent (version 7c). (2011).
[65] J. Segurado, R.A. Lebensohn, J. Llorca, C.N. Tomé, Multiscale modeling of plasticity based on embedding the viscoplastic self-consistent formulation in implicit finite elements, Int. J. Plast. 28 (2012) 124–140.
[66] S. Mercier, A. Molinari, Homogenization of elastic–viscoplastic heterogeneous materials: Self-consistent and Mori–Tanaka schemes, Int. J. Plast. 25 (2009) 1024–1048.
[67] F. Roters, P. Eisenlohr, L. Hantcherli, D.D. Tjahjanto, T.R. Bieler, D. Raabe, Overview of constitutive laws, kinematics, homogenization and multiscale methods in crystal plasticity finite-element modeling: Theory, experiments, applications, Acta Mater. 58 (2010) 1152–1211.
[68] J.W. Hutchinson, Bounds and self-consistent estimates for creep of polycrystalline materials, Proc. R. Soc. London, A (1976) 101–126.
[69] A. Ma, F. Roters, A constitutive model for fcc single crystals based on dislocation densities and its application to uniaxial compression of aluminium single crystals, Acta Mater. 52 (2004) 3603–3612.
[70] M. Knezevic, M. Zecevic, I.J. Beyerlein, J.F. Bingert, R.J. McCabe, Strain rate and temperature effects on the selection of primary and secondary slip and twinning systems in HCP Zr, Acta Mater. 88 (2015) 55–73.
[71] M. Ardeljan, I.J. Beyerlein, B.A. McWilliams, M. Knezevic, Strain rate and temperature sensitive multi-level crystal plasticity model for large plastic deformation behavior: Application to AZ31 magnesium alloy, Int. J. Plast. 83 (2016) 90–109.
[72] S. Chen, G. Gray III, S. Bingert, Mechanical properties and constitutive relations for tantalum and tantalum alloys under high-rate deformation, in: Los Alamos National Lab. NM (United States), 1996.

[73] M. Knezevic, H.F. Al-Harbi, S.R. Kalidindi, Crystal plasticity simulations using discrete Fourier transforms, Acta Mater. 57 (2009) 1777–1784.

[74] S.R. Kalidindi, C.A. Bronkhorst, L. Anand, Crystallographic texture evolution in bulk deformation processing of FCC metals, J. Mech. Phys. Solids 40 (1992) 537–569.

[75] M. Knezevic, L. Capolungo, C.N. Tomé, R.A. Lebensohn, D.J. Alexander, B. Mihaila, R.J. McCabe, Anisotropic stress–strain response and microstructure evolution of textured α-uranium, Acta Mater. 60 (2012) 702–715.

[76] M. Knezevic, R.J. McCabe, C.N. Tomé, R.A. Lebensohn, S.R. Chen, C.M. Cady, G.T. Gray Iii, B. Mihaila, Modeling mechanical response and texture evolution of α-uranium as a function of strain rate and temperature using polycrystal plasticity, Int. J. Plast. 43 (2013) 70–84.

[77] M. Knezevic, I.J. Beyerlein, D.W. Brown, T.A. Sisneros, C.N. Tomé, A polycrystal plasticity model for predicting mechanical response and texture evolution during strain-path changes: Application to beryllium, Int. J. Plast. 49 (2013) 185–198.

[78] R. McCabe, L. Capolungo, P. Marshall, C. Cady, C. Tomé, Deformation of wrought uranium: experiments and modeling, Acta Mater. 58 (2010) 5447–5459.

[79] L. Capolungo, I. Beyerlein, G. Kaschner, C. Tomé, On the interaction between slip dislocations and twins in HCP Zr, Mater. Sci. Eng. A 513 (2009) 42–51.

[80] G. Zhou, Z. Li, D. Li, Y. Peng, H.S. Zurob, P. Wu, A polycrystal plasticity based discontinuous dynamic recrystallization simulation method and its application to copper, Int. J. Plast. 91 (2017) 48–76.

[81] R.A. Lebensohn, C.N. Tomé, A self-consistent viscoplastic model: prediction of rolling textures of anisotropic polycrystals, Mater. Sci. Eng. A 175 (1994) 71–82.

[82] M. Zecevic, I.J. Beyerlein, R.J. McCabe, B.A. McWilliams, M. Knezevic, Transitioning rate sensitivities across multiple length scales: microstructure–property relationships in the Taylor cylinder impact test on zirconium, Int. J. Plast. 84 (2016) 138–159.

[83] M. Knezevic, R.J. McCabe, R.A. Lebensohn, C.N. Tomé, C. Liu, M.L. Lovato, B. Mihaila, Integration of self-consistent polycrystal plasticity with dislocation density based hardening laws within an implicit finite element framework: Application to low-symmetry metals, J. Mech. Phys. Solids 61 (2013) 2034–2046.

[84] J. Crank, P. Nicolson, A practical method for numerical evaluation of solutions of partial differential equations of the heat-conduction type, in: Mathematical Proceedings of the Cambridge Philosophical Society, Cambridge University Press, 1947, pp. 50–67.

[85] D.J. Savage, I.J. Beyerlein, M. Knezevic, Coupled texture and non-Schmid effects on yield surfaces of body-centered cubic polycrystals predicted by a crystal plasticity finite element approach, Int. J. Solids Struct. 109 (2017) 22–32.

[86] A. Patra, T. Zhu, D.L. McDowell, Constitutive equations for modeling non-Schmid effects in single crystal bcc-Fe at low and ambient temperatures, Int. J. Plast. 59 (2014) 1–14.

[87] H. Lim, L. Hale, J. Zimmerman, C. Battaile, C. Weinberger, A multi-scale model of dislocation plasticity in α-Fe: incorporating temperature, strain rate and non-schmid effects, Int. J. Plast. 73 (2015) 100–118.

[88] R. Gröger, V. Vitek, Multiscale modeling of plastic deformation of molybdenum and tungsten. III. Effects of temperature and plastic strain rate, Acta Mater. 56 (2008) 5426–5439.

[89] R. Becker, Analysis of texture evolution in channel die compression—I. Effects of grain interaction, Acta Metall. Mater. 39 (1991) 1211–1230.

[90] E. Voce, The relationship between stress and strain for homogeneous deformation, J. Inst. Met. 74 (1948) 537–562.

[91] U.F. Kocks, Laws for work-hardening and low-temperature creep, J. Eng. Mat. Technol. Trans. ASME 98 Ser H (1976) 76–85.

[92] M. Knezevic, J.S. Carpenter, M.L. Lovato, R.J. McCabe, Deformation behavior of the cobalt-based superalloy Haynes 25: Experimental characterization and crystal plasticity modeling, Acta Mater. 63 (2014) 162–168.

[93] R. Masson, M. Bornert, P. Suquet, A. Zaoui, An affine formulation for the prediction of the effective properties of nonlinear composites and polycrystals, J. Mech. Phys. Solids 48 (2000) 1203–1227.

[94] R.A. Lebensohn, C.N. Tomé, P.P. Castaneda, Self-consistent modelling of the mechanical behaviour of viscoplastic polycrystals incorporating intragranular field fluctuations, Phil. Mag. 87 (2007) 4287–4322.

[95] R.J. Asaro, J.R. Rice, Strain localization in ductile single crystals, J. Mech. Phys. Solids 25 (1977) 309–338.

[96] T.J.R. Hughes, J. Winget, Finite rotation effects in numerical integration of rate constitutive equations arising in large-deformation analysis, Internat. J. Numer. Methods Engrg. 15 (1980) 1862–1867.

[97] M. Zecevic, R.J. McCabe, M. Knezevic, Spectral database solutions to elasto-viscoplasticity within finite elements: application to a cobalt-based FCC superalloy, Int. J. Plast. 70 (2015) 151–165.

[98] M. Zecevic, R.J. McCabe, M. Knezevic, A new implementation of the spectral crystal plasticity framework in implicit finite elements, Mech. Mater. 84 (2015) 114–126.

[99] J.C. Simo, Numerical analysis and simulation of plasticity, Handb. Numer. Anal. 6 (1998) 183–499.

[100] R. Goetz, S. Semiatin, The adiabatic correction factor for deformation heating during the uniaxial compression test, JMEP 10 (2001) 710–717.

[101] P. Knysh, Y.P. Korkolis, Determination of the fraction of plastic work converted into heat in metals, Mech. Mater. 86 (2015) 71–80.

[102] R. Kapoor, S. Nemat-Nasser, Determination of temperature rise during high strain rate deformation, Mech. Mater. 27 (1998) 1–12.

[103] D. Rittel, A. Bhattacharyya, B. Poon, J. Zhao, G. Ravichandran, Thermomechanical characterization of pure polycrystalline tantalum, Mater. Sci. Eng. A 447 (2007) 65–70.

[104] K.-J. Bathe, Finite Element Procedures, Prentice Hall, Englewood Cliffs, N.J, 1996.

[105] A. Prakash, W. Nöhring, R. Lebensohn, H. Höppel, E. Bitzek, A multiscale simulation framework of the accumulative roll bonding process accounting for texture evolution, Mater. Sci. Eng. A 631 (2015) 104–119.

[106] K. Shoemake, Animating rotation with quaternion curves, in: ACM SIGGRAPH Computer Graphics, ACM, 1985, pp. 245–254.

[107] M. Knezevic, N.W. Landry, Procedures for reducing large datasets of crystal orientations using generalized spherical harmonics, Mech. Mater. 88 (2015) 73–86.
[108] B.E. Hollister, A. Pang, Interpolation of non-Gaussian probability distributions for ensemble visualization, in: Proc. IEEE Vis. Posters, 2013.
[109] N. Bonneel, M. Van De Panne, S. Paris, W. Heidrich, Displacement interpolation using Lagrangian mass transport, in: ACM Transactions on Graphics (TOG), ACM, 2011, p. 158.
[110] F.H. Bursal, On interpolating between probability distributions, Appl. Math. Comput. 77 (1996) 213–244.
[111] V. Sundararaghavan, N. Zabaras, Linear analysis of texture–property relationships using process-based representations of Rodrigues space, Acta Mater. 55 (2007) 1573–1587.
[112] M. Miller, T. Turner, A methodology for measuring and modeling crystallographic texture gradients in processed alloys, Int. J. Plast. 17 (2001) 783–805.
[113] S.R. Chen, G.T. Gray III, Constitutive behavior of tungsten and tantalum: experiments and modeling, in: Proceedings of the 2nd International Conference on Tungsten and Refractory Metals, Metal Powders Industries Federation, Princeton, New Jersey, 1995, pp. 489–498.
[114] I. Dillamore, W. Roberts, Preferred orientation in wrought and annealed metals, Metall. Rev. 10 (1965) 271–380.
[115] I. Dillamore, H. Katoh, K. Haslam, The nucleation of recrystallisation and the development of textures in heavily compressed iron-carbon alloys, Texture, Stress, Microstruct. 1 (1974) 151–156.
[116] R.A. Lebensohn, N-site modeling of a 3D viscoplastic polycrystal using Fast Fourier Transform, Acta Mater. 49 (2001) 2723–2737.
[117] M. Zecevic, W. Pantleon, R.A. Lebensohn, R.J. McCabe, M. Knezevic, Predicting intragranular misorientation distributions in polycrystalline metals using the viscoplastic self-consistent formulation, Acta Mater. 140 (2017) 398–410.
[118] R.A. Lebensohn, M. Zecevic, M. Knezevic, R.J. McCabe, Average intragranular misorientation trends in polycrystalline materials predicted by a viscoplastic self-consistent approach, Acta Mater. 104 (2016) 228–236.